Astroglial-Kir4.1 in Lateral Habenula Drives Neuronal Bursts to Mediate Depression

Yihui Cui, Yan Yang, Zheyi Ni, Yiyan Dong, Guohong Cai, Alexandre Foncelle, Shuangshuang Ma, Kangning Sang, Siyang Tang, Yuezhou Li, et al.

Astroglial-Kir4.1 in Lateral Habenula Drives Neuronal Bursts to Mediate Depression

Yihui Cui[1], Yan Yang[1], Zheyi Ni[1], Yiyan Dong[1], Guohong Cai[3], Alexandre Foncelle[4], Shuangshuang Ma[1], Kangning Sang[1], Siyang Tang[1], Yuezhou Li[1], Ying Shen[1], Hugues Berry[4], Shengxi Wu[3], Hailan Hu[1,2*]

[1]Center for Neuroscience, Key Laboratory of Medical Neurobiology of the Ministry of Health of China, School of Medicine, Interdisciplinary Institute of Neuroscience and Technology, Qiushi Academy for Advanced Studies, Zhejiang University, Hangzhou 310058, P.R. China

[2] Mental Health Center, School of Medicine, Zhejiang University, Hangzhou 310013, P.R. China

[3]Department of Neurobiology, Fourth Military Medical University, Xi'an, 710032, P.R. China

[4]INRIA, France; University of Lyon, France

[*]Author for correspondence: huhailan@zju.edu.cn

Tel: +86-(0)571-8898-1720

Fax: +86-(0)571-8820-8920

Keywords: depression, lateral habenula, bursting, Kir4.1, inward-rectifying potassium channel, astrocyte, neuron-glia interaction, potassium buffering, firing mode

Summary

Enhanced bursting activity of the lateral habenula (LHb) neurons is essential in driving depressive-like behaviors, but the cause of this increased bursts remained unknown. Here using high-throughput quantitative proteomic screen, we identified an astroglial potassium channel, Kir4.1, to be upregulated in the LHb of animal models of depression. Kir4.1 in the LHb shows a distinct expression pattern on the astrocytic membrane processes tightly wrapping around the neuronal soma. Electrophysiology and modeling data demonstrate that the level of Kir4.1 on astrocytes tightly regulates the degree of membrane hyperpolarization and the amount of burst activity of LHb neurons. Astrocyte-specific gain and loss of Kir4.1 functions in the LHb bidirectionally regulate neuronal bursting and depressive-like symptoms. Together, these results reveal a new form of glial-neural interaction in setting neuronal firing mode in a devastating psychiatric disease, and discover the therapeutic potential of targeting LHb Kir4.1 for treating major depression.

A major breakthrough in neuroscience has been the discovery that astrocytes intimately interact with neurons to support and regulate a series of essential functions to foster brain information processing[1-7]. A wealth of investigations has focused on the astroglial-neural interactions at the tripartite synapses, where astrocyte processes tightly wrap around pre- and post-synaptic sites[8]. In contrast, not as much attention has been placed on astroglial-neural interaction in proximity to neuronal soma[9,10]. Particularly, how astrocytes regulate intrinsic firing patterns of neurons, and what structural basis may underlie this regulation, are much less explored.

Despite the surging interest of lateral habenula (LHb) in negative emotion[11-20], only limited attention has been given to astrocytes and their potential roles in LHb hyperfunction in depression[21]. In the accompanying paper, we demonstrate that bursting activity of LHb neurons are greatly enhanced in animal models of depression. LHb burst drives depressive-like behaviors and is a prominent target of the rapid antidepressant ketamine. However, the cause of this enhanced burst of LHb neurons remains unsolved.

Results

Kir4.1 is upregulated in LHb of animal models of depression

In an unbiased, high-throughput, quantitative proteomic screening to compare habenular protein expression of congenitally learned helpless (cLH) rats[22] and wild-type SD rats, we identified Kir4.1 to be highly upregulated in the LHb of cLH rats[11] (1.69-fold of wild-type control, $p = 0.02$, Student's *t*-test, Fig. 1a). Western blot analysis confirmed that Kir4.1 had a significant increase (1.44-fold, $p = 0.009$, Paired *t*-test) in the membrane protein extraction of cLH habenulae (Fig. 1b). In contrast, another astrocyte-specific protein, glial fibrillary acidic protein (GFAP), did not show any change in expression (Extended Data Fig. 1a), indicating there was no astrogliosis.

To test whether Kir4.1 upregulation is universal in depression, we examined an additional rat model of depression, the LPS (lipopolysaccharide)-induced depression[23]. One week of LPS injection (0.5mg/kg, i.p.) in 3-month-old Wistar rats was sufficient to cause strong depressive-like phenotype in the forced swim test (FST, Extended Data Fig. 2e)[23] and sucrose preference test (SPT)[23]. The Kir4.1 level was also significantly increased in the LPS-induced rats (1.87-fold, $p < 0.0001$, Paired *t*-test, Fig. 1c). Quantitative real-time PCR revealed an increase (1.2-fold, $p = 0.015$, Paired *t*-test) of Kir4.1 mRNA level in cLH habenulae (Fig. 1d), suggesting that at least part of the protein level change is due to transcriptional upregulation.

Age-dependent increase of LHb astrocytic Kir4.1 current and depression onset in cLH rats

Kir4.1 is a principal component of the glial Kir channel and is largely responsible for mediating the K+ conductance and setting the resting membrane potential (RMP) of astrocytes[24]. To confirm that Kir4.1 function is indeed upregulated, we performed whole-cell patch clamp onto the astrocytes in brain slices made from the LHb of cLH or SD rats. Astrocytes were distinguished from neurons by their small (5–10 μm) oval shaped somata and electrophysiological features including a relatively hyperpolarized RMP (−74 ± 1 mV), a low input resistance Rin (47 ± 6 MΩ), a linear I–V relationship and an absence of action potentials in response to depolarizing current injections (Extended Data Fig. 2a-d)[25-27]. Biocytin filling and absence of NeuN co-staining confirmed that cells fitting the above criteria were indeed astrocytes (Extended Data Fig.3). We then bath applied Ba^{2+} ($BaCl_2$, 100 μM), which selectively blocks Kir channels at sub-mM concentrations, to isolate Kir4.1 current[25] (Extended Data Fig. 2a, c). The Ba^{2+}-sensitive current displayed a reversal potential close to Ek (-90mV)[25,28] (Fig. 1e, f), indicating that it represents the K+ conductance. We

found that Ba^{2+}-sensitive currents in LHb astrocytes were almost doubled in cLH rats (Fig. 1e), as well as in LPS-treated rats (Extended Data Fig. 2f), at the age of P60-90.

Interestingly, the increase of Kir4.1 current and protein level was not obvious at P30 (Fig. 1f, Extended data Fig. 1b). At this age, cLH rats did not yet show depressive-like phenotypes in both the FST (Fig. 1g) and learned helpless test (LHT, Fig. 1h), suggesting that the upregulation of Kir4.1 level is concomitant with the developmental onset of the depressive-like symptoms.

Kir4.1 are expressed on astrocytic processes tightly wrapping around neuronal soma

As an inwardly rectifying K+ channel, Kir4.1 has been strongly implicated in buffering excess extracellular K+ in tripartite synapses[24,29-31]. Conventional model of K+ buffering suggests Kir4.1 to be highly expressed in astrocytic endfeet surrounding synapses[32-34]. Surprisingly, with immunohistochemistry co-labeling, Kir4.1 staining in LHb appeared to overlap with the neuronal marker NeuN at low magnification (20X, Extended Data Fig. 4a), although in the same brain slice Kir4.1 staining patterns in hippocampus were typical astrocytic-looking (Extended Data Fig. 4b). However, higher magnification imaging with single layer scanning (0.76μm per layer) revealed that Kir4.1 staining enveloped NeuN signals (Fig. 2a). To confirm that Kir4.1 indeed locates within astrocytes but not neurons in LHb, we separately knocked it out in either neurons or astrocytes by injecting AAV virus expressing the cre recombinase under either the neuronal promoter CaMKII or glial promoter GFAP (gfaABC1D)[26,35] into $Kir4.1^{f/f}$ floxed mice[25]. The staining of Kir4.1 remained intact with neuronal knock-out, but was completely eliminated with astrocytic knock-out (Fig. 2b). Electron microscopy imaging revealed that Kir4.1-positive gold particles were distributed encircling the membrane of neuronal cell bodies (Fig. 2c, Extended Data Fig. 5a, b), as well

as in the synapses (Extended Data Fig. 5d). Consistently, whole-cell-patch recordings showed that Ba^{2+}-sensitive currents were absent in neurons but abundant in astrocytes in the LHb (Fig. 2d, Extended Data Fig. 6). Together these results suggest that Kir4.1 is mainly expressed in astrocytic processes tightly wrapping around neuronal soma and synapses in the LHb.

Overexpression of kir4.1 in LHb astrocytes increases neuronal bursts and causes strong depressive-like behaviors

To test the consequence of Kir4.1 upregulation in LHb, we used adeno-associated viruses of the 2/5 serotype (AAV2/5) that preferentially target astrocytes[26] together with the human GFAP (gfaABC1D) promoter[26,35] to deliver GFP-tagged Kir4.1 channels (AAV-GFAP::Kir4.1) or AAV-GFAP::GFP as a control (Fig. 3a). 14 days after bilateral injection in the LHb at P50, AAV2/5-mediated viral transfection led to Kir4.1 and GFP expression in astrocytes throughout the LHb (Fig. 3b). The specificity of the viral infection in astrocytes was verified by co-immunostaining of NeuN and GFP: only 0.3% NeuN+ cells (n = 2668) were infected by this virus (Extended Data Fig.7). We made whole-cell recordings from either astrocytes or neurons surrounding the viral-transfected astrocytes in coronal LHb slices (Fig. 3c-e). The RMPs of both astrocytes and neurons were more hyperpolarized (Fig. 3d, e) and the percentage of bursting neurons were significantly higher (Fig.3f) in mice infected with AAV-GFAP::Kir4.1 than with AAV-GFAP::GFP.

We then assayed depressive-like phenotypes and found that mice with AAV-GFAP::Kir4.1 infection in the LHb displayed severe depressive-like behaviors, including increased immobile duration ($p = 0.0002$, Unpaired *t*-test) and decreased latency to immobility ($p = 0.001$, Unpaired *t*-test) in FST (Fig. 3g), and decreased sucrose preference in the SPT ($p <$

147 0.0001, Unpaired *t*-test, Fig. 3h), while the general locomotion was unchanged (Extended
148 Data Fig. 8a-b).
149
150 **Kir4.1-mediated K buffering regulates neuronal RMP and bursting activity**
151 How does an astrocytic potassium channel regulate RMP and burst firing of the LHb neuron?
152 We hypothesize that within the highly confined extracellular space between neuronal soma
153 and Kir4.1-positive astrocytic processes (Fig. 2), the constantly-released K+ from
154 intrinsically active LHb neurons is quickly cleared by astrocytes through a Kir4.1-dependent
155 mechanism. Accordingly, we predict that blockade of Kir4.1 should compromise K+ spatial
156 buffering, resulting in increased extracellular K+ (Kout), and according to Nernst Equation,
157 depolarized neuronal RMPs (modeled in Extended Data Fig. 9). Consistent with this
158 prediction, blocking Kir4.1 with $BaCl_2$ depolarized the RMPs of LHb neurons, after about 10
159 min bath perfusion of $BaCl_2$ (Fig. 4a). The amount of changes in RMP positively correlated
160 with the original firing rates of neurons (Fig. 4b), indicating that the more active the neuron is,
161 the larger contribution the K+ buffering to its RMP. Similar amount of RMP change was
162 induced when BaCl2 was applied in presence of synaptic transmission blockers (picrotoxin,
163 NBQX and AP5, Extended Data Fig. 10), suggesting that Kir4.1-dependent regulation of
164 LHb neuronal RMP occurs mostly at neuronal cell bodies instead of at synaptic sites.
165 Consequent to the RMP change, perfusion of $BaCl_2$ caused a dramatic increase of firing
166 frequency until the neuron reached a sustained plateau of a tetanus response and stopped
167 firing (Fig. 4c).
168
169 Vice versa, upregulation of Kir4.1 or stop neuronal firing should decrease extracellular K+
170 (Kout) and hyperpolarize neuronal RMPs. Indeed, overexpression of Kir4.1 in astrocytes (Fig.
171 3e) or blocking neuronal APs by TTX (Fig. 4d, e) both caused hyperpolarization of LHb

neurons. Overexpression of Kir4.1 in astrocytes also increased neuronal bursts (Fig. 3g). Finally, to assess a causal relationship between Kout and firing mode, we made current-clamp recordings of LHb neurons while lowering Kout from 2.75mM to 1.4mM (Fig. 4f). This led to lowered neuronal RMP by 13.7 +/- 0.5mV and a direct shift of originally tonic-firing neurons (8 out of 15) into bursting mode (Fig. 4g). Consequently, percentage of bursting neurons was increased from 8% to 23% ($p < 0.0001$, Chi-square test, Fig. 4h). In summary, by increasing astrocytic Kir4.1 expression or decreasing the extracellular K+ concentration, we were able to phenocopy in WT animals several key neuronal properties observed in the LHb of animal models of depression, namely hyperpolarized RMPs and enhanced bursts. These results indicate that enhanced capacity of extracellular K clearance due to Kir4.1 overexpression may underlie the neuronal hyperpolarization required for burst initiation.

Loss-of-function of Kir4.1 in LHb decreases neuronal bursting and rescues depressive-like phenotypes

Next, to determine whether loss-of-function of Kir4.1 in the LHb may reduce neuronal bursts and reverse depressive phenotypes, we devised two strategies, by using AAV2/5 viral vectors to express either a short hairpin RNA (shRNA) to knock down the level of Kir4.1, or a dominant negative construct to block its function in the LHb of cLH rats (Fig. 5a). We tested six shRNAs specifically targeting the Kir4.1 transcript in cell culture and chose the one with most efficient knock-down efficiency (Fig. 5b and Extended Data Fig. 11a) for viral package. To avoid an off-target effect of shRNA, we also used a dominant-negative form of Kir4.1, dnKir4.1, containing a GYG to AAA point mutation at the channel pore, which blocks K^+ channels[36] (Extended Data Fig. 11b, 12, Fig. 5c). We first examined the effect of Kir4.1-shRNA on glial and neural electrophysiological properties. In astrocytes infected with the

AAV-H1::Kir4.1-shRNA, we observed a dramatic change of I-V relation (Fig. 5d), a 32 mV depolarization compared with non-infected astrocytes ($p < 0.0001$, One-way ANOVA) and 41mV depolarization compared with ctrl-shRNA-infected astrocytes ($p < 0.0001$, One-way ANOVA, Fig. 5e), consistent with the literature that Kir4.1 is majorly responsible for setting the astrocytic RMPs[25]. In neurons infected with the AAV-H1::Kir4.1-shRNA, the RMPs did not differ from neighboring non-infected neurons (because neurons do not express Kir4.1 endogenously, Fig. 5f). However, RMPs of neighboring LHb neurons from AAV-H1::Kir4.1-shRNA-infected brain slices were overall more depolarized than RMPs of those from AAV-H1::Ctrl-shRNA-infected rats (-43 ± 2mV vs. -53 ± 2.7mV, $p = 0.006$, One-way ANOVA, Fig. 5f), suggesting that knock-down of Kir4.1 in astrocytes had a global impact on RMPs of neighboring neurons. Similar effects were observed in AAV-GFAP::dnKir4.1 infected LHb slices (Extended Data Fig. 11c-f). Most importantly, bursting activity in the LHb of cLH rats were significantly eliminated by AAV-H1::Kir4.1-shRNA (Fig. 5g) and AAV-GFAP::dnKir4.1 (Extended Data Fig. 11f) infection.

Behaviorally, infection of AAV-H1::Kir4.1-shRNA or AAV-GFAP::dnKir4.1 had a pronounced effect on rescuing the depressive-like phenotypes of cLH rats in three depression paradigms: reducing the immobility time ($p = 0.01$, Unpaired *t*-test, Fig. 5h) and increasing latency to immobility ($p = 0.0018$, Unpaired *t*-test, Fig. 5h) in FST, increasing bar pressing number in the LHT ($p = 0.0004$, Unpaired *t*-test, Fig. 5i, j), and increasing the sucrose preference score in SPT ($p = 0.04$, Unpaired *t*-test, Fig. 5k). The behavior scores in LHT clearly correlated with those in FST (Fig. 5l).

Here we discover an important function of Kir4.1 at the highly specialized neuron-glia interface in the LHb in regulating neuronal RMP and firing pattern. During depression, the

upregulation of Kir4.1 may cause enhanced capacity of extracellular K clearance, leading to a decrease of Kout and neuronal hyperpolarization (Fig. 5m). As demonstrated in our accompanying manuscript, neuronal hyperpolarization may de-inactivate T-type voltage-sensitive calcium channels (T-VSCCs) which in turn initiate NMDAR-dependent bursts to cause a stronger suppression of the downstream monoaminergic centers (Fig. 5m). These results may inspire the development of novel treatments of major depression targeting on maladaptive neuron-glia interactions in the LHb.

Acknowledgements

We thank Dr. Ken McCarthy for gift of Kir4.1$^{f/f}$ floxed mice; Baljit Khakh for GFAP-Kir4.1 plasmid; Jianhong Luo for HEK293 cells; Guangping Gao for AAV-GFAP::GFP; Tian Xue for advice on dn-Kir4.1 design; Yingying Liu for technical support on electromicroscopy experiment; Chenjie Shen for help with immunohistochemistry; Yudong Zhou, Shumin Duan, Jingwei Zhao and Xiaohui Zhang for advices on experimental design; Christian Giaum and Pierre Magistretti for comments on manuscript. Patent applied for 201710322245.X. This work was supported by grants from the Ministry of Science and Technology of China (2016YFA0501000), the National Natural Science Foundation of China (91432108, 31225010, and 81527901), the Strategic Priority Research Program (B) of the Chinese Academy of Sciences (XDB02030004), 111 project (B13026) to H. H..

Author contributions

H.H. and Y.C. designed the study. Y.C. performed the *in vitro* patch recordings; Y.Y. performed the biochemistry and immunohistochemistry experiments; Y.C., Y.Y., Y.D. and K.S. performed viral injections and behavioral experiments; Z.N., A.F. and H.B. established

248 the biophysical model; S.M. assisted cell culture experiments; G.C. and S.W. conducted the
249 EM experiments; Y.S. contributed Kir4.1$^{f/f}$ floxed mice; S.T. and Y.L. constructed plasmids.
250 H.H. wrote the manuscript with the assistance of Y.C., Y.Y. and Z.N..
251

Methods

Animals. Male cLH rats (3-4 weeks or 8-12 weeks of age) and age-matched male Sprague Dawley rats (SLAC Laboratory Animal Co., Shanghai) were used. The cLH rats were screened by learned helpless test[1,2] for breeding as previously described[1]. Male Wistar rats (SLAC Laboratory Animal Co., Shanghai, 12 weeks) were used for establishing the LPS-induced depressive-like rat model. Male adult (7-8 weeks of age) C57BL/6 mice (SLAC) or Kir4.1$^{f/f}$ floxed mice (originally obtained from Dr. Ken McCarthy at University of North Carolina) were used for virus injection the immunohistochemistry experiments. Animals were group-housed two/cage for rats and four/cage for mice under a 12-h light-dark cycle (light on from 7 a.m. to 7 p.m.) with free access to food and water *ad libitum*. All animal studies and experimental procedures were approved by the Animal Care and Use Committee of the animal facility at Zhejiang University.

Western Blot. The habenular membrane fraction and whole protein was extracted as previously described[11]. Animals were anesthetized using 10% chloral hydrate, and habenular tissue was quickly dissected from the brain and homogenized in lysis buffer (320 mM sucrose, 4 mM HEPES pH7.4, 1 mM $MgCl_2$ and 0.5 mM $CaCl_2$, 5 mM NaF, 1 mM Na_3VO_4, EDTA-free, Protease Inhibitor cocktail tablets (Roche) on ice. The lysis buffer used for extracting the total protein of HEK293TN cell contained 50mM Tris (pH 7.4), 150mM NaCl, 1% Triton X-100, 1% sodium deoxycholate, 0.1% SDS and Protease Inhibitor cocktail tablets (Roche). After protein concentration measurement by BCA assay, 10~20μg proteins for each lane was separated on a 10% SDS-PAGE gel and transferred for western blot analysis. Anti-Kir4.1 (1:1000, Alomone labs), anti-GFAP (1:1000, Sigma) and anti-tubulin (1:5000, Bio-Rad) antibodies, and high sensitive ECL reagent (GE Healthcare) were used. All the bands were analyzed with Quantity one or Image J.

Immunohistochemistry. Animals were anesthetized using 10% chloral hydrate, and then perfused transcardially with ice-cold PBS (pH 7.4) followed by 4% paraformaldehyde. After overnight post fix in 4% paraformaldehyde solution, brains were cryoprotected in 30% sucrose for 1 day (for mice) or 3 days (for rats). Coronal sections (40 μm) were cut on a microtome (Leica) and collected in PBS and stored at 4°C for further using. The antibodies used were rabbit anti-Kir4.1 extracellular peptide (1:200, Alomone labs), mouse anti-GFAP (1:500, Sigma), mouse anti-NeuN (1:500, Millipore), Rabbit anti NeuN (1:500, Millipore), mouse anti-S100b (1:500, Sigma), chicken anti-GFP (1:1000, Abcam), Mouse anti-Flag (1:1000, Beyotime), Alexa Fluor 488 goat anti-rabbit IgG, Alexa Fluor 488 goat anti-chicken IgG, Alexa Fluor 546 goat anti-mouse IgG (all 1:1000, Invitrogen). Specifically, for Kir4.1 staining, the rabbit anti-Kir4.1 extracellular peptide antibody was incubated for 48-72 h and the other primary antibodies were incubated for 36-48 h. For the antibody absorption experiments, the rabbit anti-Kir4.1 extracellular peptide antibody was pre-adsorbed with the Kir4.1 antigen by mixing at the weight ratio of 1:2 for 24 h. Slices were counterstained with Hoechst in the final incubation step to check the injection site. Fluorescent image acquisition was performed with an Olympus Fluoview FV1000 confocal microscope and a Nikon A1 confocal microscope.

Cell transfection and cell culture. HEK293 cells (gift from Jianhong Luo) were used for the electrophysiology recording and HEK293TN cells (Taitool Bioscience, China) were used for western blot analysis. Cells used in this study were authenticated and checked for mycoplasma contamination. The plasmids used were pAAV-Ubi-Kir4.1-2A-eGFP, pAAV-Ubi-dnKir4.1 (GYG to AAA)-2A-eGFP, pAAV-CAG-eGFP, pAAV-H1-Kir4.1-shRNA-CAG-eGFP and pAAV-H1-Luciferase-shRNA-CAG-eGFP. HEK293 cells were trypsinized for 5 min using 0.25% trypsin (wt/vol), and replated onto glass coverslips in fresh

DMEM:F12 medium (Life Technologies) containing 1 mM nonessential amino acids (Gibco), 1 mM sodium pyruvate (Gibco), and 10% FBS (Hycolone). Cells were transfected using Lipofectamine 2000 (Invitrogen) according to standard protocols, then cultured for 5-6 h in well plates at 37 ºC in a humid atmosphere of 5% CO_2 and 95% air. Cells were cultured for another 48 h before western blot or electrophysiology experiments.

Plasmid constructs. The pAAV-Ubi-Kir4.1-2A-eGFP plasmid was assembled by homologous recombination of AAV backbone linearized from the AAV-Ubi-CaMKII-2A-eGFP plasmid[11] by PCR and Kir4.1 amplified from pZac2.1- gfaABC1D-EGFP-Kir4.1 plasmid (AddGene). The pAAV-Ubi-dnKir4.1 (GYG to AAA)-2A-eGFP plasmid was made by PCR-based mutagenesis using pAAV-Ubi-Kir4.1-2A-eGFP as a backbone (Fw: 5'-AAAGATGGCCGGAGCAACGTGAGAATGGAGCATATTGCT-3'; Rev: 5'-GCTGATGTAGCGGAAGGCGGCGGCAATGGTGGTCTGGGATTCGAGGGA-3'). The pAAV-gfaABC1D- dnKir4.1 (GYG to AAA)-2A-EGFP was assembled by homologous recombination of pZac2.1 gfaABC1D backbone linearized from the pZac2.1- gfaABC1D-EGFP-Kir4.1 plasmid (AddGene) by PCR and Kir4.1dn-2A-EGFP sequence amplified from pAAV-Ubi-dnKir4.1 (GYG to AAA)-2A-eGFP plasmid. The pAAV-H1-Kir4.1-shRNA-CAG-eGFP was constructed using a vector (provide by Taitool Bioscience, China), which contains a CAG promoter driving eGFP and a H1 promoter driving shRNA expression. We designed 6 shRNA sequences by RNAi designer online software (Invitrogen) as indicated below:

1) 5'-GGACGACCTTCATTGACAT-3';
2) 5'-GCTACAAGCTTCTGCTCTTCT-3';
3) 5'-GCTCTTCTCGCCAACCTTTAC-3';
4) 5'-CCGGAACCTTCCTTGCAAA-3';

5) 5’-GCGTAAGAGTCTCCTCATTGG-3’

6) 5’-GCCCTTAGTGTGCGCATTA-3’.

We then tested the knock-down efficiency by Western blot of Kir4.1 from HEK293TN cells which were co-transfected with Flag-tagged-Kir4.1 plasmid (pAAV-CMV-betaGlobin-Kir4.1-eGFP-3Flag) and each of the six shRNA plasmids. Based on our western blot result (Extended Figure 11a), we chose the fifth sequence, 5’-GCGTAAGAGTCTCCTCATTGG-3’, for Kir4.1-shRNA virus package.

Electron microscopic immunohistochemistry. Four mice were deeply anesthetized with 1% sodium pentobarbital intraperitoneally (50 mg/kg body weight) and perfused transcardially with 20ml saline, followed by 40ml ice-cold mixture of 4% paraformaldehyde and 0.05% glutaraldehyde in 0.1M PB for 1 h. Brainstems were removed and postfixed by immersion in the same fixative for 4 h at 4ºC. Serial coronal sections of 50 μm thickness were prepared with a vibratome (VT 1000S, Leica), and approximately 18-20 sections, including the LHb region, were collected from each brain.

Kir4.1 was detected by the immunogold-silver staining. Briefly, sections were blocked with blocking buffer (5% BSA, 5% NGS and 0.05% Triton X-100 in PBS), and then incubated overnight in the primary antibodies of rabbit anti-Kir4.1 (1:200) diluted with solution containing 1% BSA, 1% NGS and 0.05% Triton X-100.The secondary antibody was anti-rabbit IgG conjugated to 1.4 nm gold particles (1:100, Nanoprobes, Stony Brook, NY) for 4 h. After rinsing, sections were post fixed in 2% glutaraldehyde in PBS for 45 min. Silver enhancement was performed in the dark with HQ Silver Kit (Nanoprobes) for visualization of Kir4.1 immunoreactivity. Before and after the silver enhancement step, sections were rinsed several times with de-ionized water.

Immuno-labeled sections were fixed with 0.5% osmium tetroxide in 0.1 M PB for 1 h, dehydrated in graded ethanol series, then in propylene oxide, and finally flat-embedded in Epon 812 between sheets of plastic. After polymerization, acrylic sheets were then pealed from the polymerized resin, and flat-embedded sections were examined under the light microscope. Three to four sections containing Kir4.1 immunoreactivity in the LHb were selected from each section, trimmed under a stereomicroscope, and glued onto blank resin stubs. Serial ultrathin sections were cut with an Ultramicrotome (Leica EM UC6, Germany) using a diamond knife (Diatome, PA) and mounted on formvar-coated mesh grids (6-8 sections/grid). They were then counterstained with uranyl acetate and lead citrate, and observed under a JEM-1230 electron microscope (JEOL LTD, Japan) equipped with CCD camera and its application software (832 SC1000, Gatan, PA).

Stereotaxic surgery and virus injection. cLH rats (postnatal 50-60 days) were deeply anesthetized by using 4% pentobarbital. Mice (postnatal 50-60 days) were deeply anesthetized by ketamine (100 mg/kg of body weight) and xylazine (8 mg/kg). Animals were placed on a stereotactic frame (RWD Instruments, China). A small volume of virus was injected into bilateral LHb (for rats LHb: AP, -3.7 mm from bregma; ML, ±0.7 mm; DV, -4.55 mm from the brain surface; for mice: AP, -1.72 mm from bregma; ML, ±0.46 mm; DV, -2.62 mm from the brain surface) using a pulled glass capillary with a pressure microinjector (Picospritzer III, Parker, USA) at a slow rate of 0.1 μl/min. After the injection was completed, the capillary was left for an additional 10 minutes before it was then slowly withdrawn completely. After surgery, animals were recovered from anesthesia under a heat pad.

AAV-CaMKII:EGFP-Cre (AAV2/1-CamKII-HI-EGFP-Cre, 0.2 μl, bilateral into LHb, University of Pennsylvania vector core, Pennaylvania, USA), AAV2/5-GFAP::EGFP-Cre (AAV2/5-gfaABC1D-EGFP-Cre, titer: 4.74×10^{12} v.g./ml, dilution: 1:2, 0.2 μl, bilateral into LHb, Taitool Bioscience, China), AAV-GFAP::Kir4.1 (AAV2/5-gfaABC1D-EGFP-Kir4.1, titer: 9.19×10^{12} v.g./ml, dilution: 1:5, 0.2 μl, bilateral into LHb, Taitool Bioscience, China), AAV-GFAP::GFP (AAV2/5-gfaABC1D-EGFP, titer: 1.61×10^{13} v.g./ml, dilution: 1:5, 0.2 μl, bilateral into LHb, University of Massachusetts, Guangping Gao Lab, USA), AAV-H1::Kir4.1-shRNA (AAV2/5-H1-Kir4.1-shRNA-CAG-EGFP, titer: 3.04×10^{13} v.g./ml, dilution: 1:10, 0.2 μl, bilateral into LHb, Taitool Bioscience, China), AAV-H1::Ctrl-shRNA (AAV2/5-H1-Luciferase-shRNA-CAG-EGFP, titer: 1.46×10^{13} v.g./ml, dilution: 1:5, 0.2 μl, bilateral into LHb, Taitool Bioscience, China), AAV2/5-gfaABC1D-dnKir4.1-2A-EGFP (GYG to AAA) (titer: 4.15×10^{13} v.g./ml, 0.2 μl, bilateral into LHb, Taitool Bioscience, China). All viral vectors were aliquot and stored at -80 ºC until use.

Depression model and Behavior assay

LPS-induced depression. The LPS-induced depression model was conducted as previously described[22]. Wistar male rats (3 months) were used for the experiments. LPS (Sigma, L-2880) dissolved in sterile 0.9% saline was intraperitoneally injected into Wistar rats, at a dosage of 0.5 mg/kg. This dosage was used to stimulate a subclinical infection without inducing obvious inflammation and other apparent impairments in animals. Saline or LPS was injected between 09:30 and 10:30 a.m. daily for 7 days. The forced swim test was performed 24 hours after the last injection. The habenular tissue was dissected 24 hours after the behavioral test and eletrophysiology experiments.

Learned helpless test (LHT). Male juvenile (P30) or adult (P90) cLH rats were tested in a lever-pressing task to evaluate the learned helpless (LH) phenotype[11]. A cue-light-illuminated lever in the shock chamber was presented, which can terminate the shock when rats pressed the lever. 15 escapable shocks (0.8 mA) were delivered with a 24 s inter-shock interval. Each shock lasted up to 60 s unless the rat pressed the lever to terminate the shock. Out of the 15 trials, rats which failed to press the lever for more than 10 trials were defined as "learned helplessness" (LH), and rats with less than 5 failures were defined as "non-learned helplessness" (NLH).

Forced swim test (FST). Animals were individually placed in a cylinder (12 cm diameter, 25 cm height for mice; 20 cm diameter, 50 cm height for rats) of water (23-25 ºC) and swam for 6 min under normal light[3]. Water depth was set to prevent animals from touching the bottom by tails and hind limbs. Animal behaviors were videotaped from the side. The immobility time during the last 4 min test was counted offline by an observer blind of the animal treatments. Immobility was defined as time when animals remained floating or motionless with only movements necessary for keeping balance in the water. For rats, an additional pre-test was conducted 24 h before the test, during which rats were individually placed in a cylinder of water with conditions described above for 15 min.

Sucrose preference test (SPT). Animals were single housed and habituated with two bottles of water for 2 days, followed by two bottles of 2% sucrose for 2 days[3]. Animals were then water deprived for 24 h and then exposed to one bottle of 2% sucrose and one bottle of water for 2 h in the dark phase. Bottle positions were switched after 1 h. Total consumption of each fluid was measured and sucrose preference was defined as the ratio of sucrose consumption divided by total consumptions of water and sucrose.

Open field test (OFT). Animals were placed in the center of an arena (40 cm x 40 cm x 40.5 cm for mice; and 100 cm x 100 cm x 40 cm for rats) in a room with dim light for 10 min. A video camera positioned directly above the arena was used to track the movement of each animal (Any-maze, Stoelting, US).

LHb brain slice preparation. Rats (P25-30 or P60-90) and mice (P90) were anesthetized with isoflurane and 10% chloral hydrate, and then perfused with 20 ml ice-cold ACSF (oxygenated with 95 % O_2 + 5% CO_2) containing (mM): 125 NaCl, 2.5 KCl, 25 $NaHCO_3$, 1.25 NaH_2PO_4, 1 $MgCl_2$ and 25 Glucose, with 1 mM pyruvate added. The brain was removed as quickly as possible after decapitation and put into chilled and oxygenated ACSF. Coronal slices containing habenular (350μm- and 300μm- thickness for rats and mice, respectively) were sectioned in cold ACSF by a Leica 2000 vibratome and then transferred to ASCF at 32ºC for incubation and recovery for 1h and then transferred to room temperature. ACSF was continuously gassed with 95% O_2 and 5% CO_2. Slices were allowed to recover for at least 1 hour before recording.

In vitro **electrophysiological recording.** For LHb neuron recordings, currents were measured under whole-cell patch clamp using pipettes with a typical resistance of 5–6 MΩ filled with internal solution containing (mM) 105 K-Gluconate, 30 KCl, 4 Mg-ATP, 0.3 Na-GTP, 0.3 EGTA, 10 HEPES and 10 Na-phosphocreatine, with pH set to 7.35. For the biocytin filling, 5mg/ml biocytin was added in the internal solution. The external ACSF solution contained (in mM) 125 NaCl, 2.5 KCl, 25 $NaHCO_3$, 1.25 NaH_2PO_4, 1 $MgCl_2$ and 25 Glucose. Cells were visualized with infrared optics on an upright microscope (BX51WI, Olympus). A MultiClamp 700B amplifier and pCLAMP10 software were used for electro-physiology (Axon Instruments). The series resistance and capacitance was compensated

automatically after stable Giga seal were formed. The spontaneous neuronal activity was recorded under current-clamp (I = 0 pA) for consecutive 60 s. RMP was determined during the silent period of the neuronal spontaneous activity.

To test TTX (1 μM, Sigma) and $BaCl_2$ (100 μM, Sigma) effect onto neuronal RMP and spontaneous activity, baselines were recorded for at least for 3 min. Drug were then perfused, the arrival of the drug was precisely indicated with a bubble that was pre-added before the transition from normal ACSF to drug added ACSF. TTX effect on LHb neuronal RMP and spontaneous activity was stabilized after several minutes while $BaCl_2$ effect on neuronal RMP and spontaneous activity took more than 10 min to stabilize. We thus analyzed the drug effect of TTX and $BaCl_2$ at the time point of 5min and 15 min respectively.

Astrocytic whole-cell patch clamp and Kir4.1 current isolation. Astrocytes were distinguished from neurons by their small (5-10 μm) oval-shaped somata and by distinct electrophysiological features: a hyperpolarized RMP and a low input resistance, a linear I-V relationship and an absence of action potentials in response to increased injection currents. $BaCl_2$ (100μM, Sigma) were applied to isolate Kir4.1 current which is subtracted from the IV curve recorded from -120mV to 0mV. Biocytin (Sigma) 5mg/ml was dissolved into the patch-clamp pipette solution. After electrophysiological characterization, cells are held for at least 30 minutes in voltage clamp and constantly injected with a hyperpolarization current (500 ms, 50 pA, 0.5 Hz, 30 min) to allow biocytin filling (performed at 34 ºC). Subsequently, slices were fixed overnight in 4% paraformaldehyde at 4 ºC. The antibodies used were rabbit anti-NeuN (1:500, Millipore), Alexa Fluor 546 donkey anti-rabbit IgG (1:1000, Invitrogen), Cy2-conjugated Streptavidin (1:1000, Jackson ImmunoResearch). Fluorescent image acquisition was performed with a Nikon A1 confocal microscope.

Tri-compartment model.

Tri-compartment model was constructed including the neuron, the astrocyte and the extracellular space. The model is based on ionic fluxes between three compartments. Na^+ and K^+ voltage-gated channel, and leak channel were recruited into the neuron as:

$$dV_N/dt = (I_{app} - I_K - I_{Na} - I_{Leak,N})/c_N$$

where V_N is the neuronal membrane potential, c_N is the neuronal capacitance. I_{app} is the external current applied to the neuron.I_{Na} and $I_K$are the fast Na^+ and K^+ currents responsible for the generation of action potentials; $I_{Leak,N}$ are responsible for the neuronal resting membrane potential. Kir4.1 channel on the extracellular and vessel side and leak channel were recruited into the astrocyte as:

$$dV_A/dt = (-I_{Kir} - I_{Kir\_vess} - I_{Leak,A})/c_A$$

where V_A is the astrocytic membrane potential, c_A is the astrocytic capacitance. I_{Kir} are outward during the resting state, while become inward when K^+ equilibrium potential exceeds the astrocytic membrane potential. I_{Kir_vess} accounts for the K^+ outflow from the astrocyte from the vessel side. $I_{Leak,A}$ are responsible for the astrocytic resting membrane potential.

The equations of the K^+ in the three compartments are described by:

$$d[K^+]_o/dt = (I_{kir} + I_k)/(F \cdot vol_O) - 2 \cdot (i_{pump,N} + i_{pump,A}) - d_{K\_O} \cdot ([K^+]_o - K_{O\_0})$$

$$d[K^+]_N/dt = -I_k/(F \cdot vol_N) + 2 \cdot i_{pump,N} \cdot vol_O/vol_N - d_{K\_N} \cdot ([K^+]_N - K_{N\_0})$$

$$d[K^+]_A/dt = (-I_{kir} - I_{kir\_vess})/(F \cdot vol_A) + 2 \cdot i_{pump,A} \cdot vol_O/vol_A - d_{K\_A} \cdot ([K^+]_A - K_{A\_0})$$

The extracellular K^+ is mainly contributed by I_K. Released extracellular K^+ from the neuron is taken up by through Kir4.1 channels and Na^+/K^+ pump.

The equations of the Na^+ in the three compartments are described by:

$$d[Na^+]_o/dt = I_{Na}/(F \cdot vol_O) + 3 \cdot (i_{pump,N} + i_{pump,A}) - d_{Na\_O} \cdot ([Na^+]_o - Na_{O\_0})$$

$$d[Na^+]_N/dt = -I_{Na}/(F \cdot vol_N) - 3 \cdot i_{pump,N} \cdot vol_O/vol_N - d_{Na\_N} \cdot ([Na^+]_N - Na_{N\_0})$$

$$d[Na^+]_A/dt = -3 \cdot i_{pump,A} \cdot vol_O/vol_A - d_{Na\_A} \cdot ([Na^+]_A - Na_{A\_0})$$

See supplementary information for detailed formulas.

Statistical analyses. Required sample sizes were estimated based on our past experience performing similar experiments. Animals were randomly assigned to treatment groups. Analyses were performed in a manner blinded to treatment assignments in all behavioral experiments. Statistical analyses were performed using GraphPad Prism software v6. By pre-established criteria, values were excluded from the analyses if the viral injection or drug delivering sites were out of LHb. All statistical tests were two-tailed, and significance was assigned at $P < 0.05$. Normality and equal variances between group samples were assessed using the D'Agostino & Pearson omnibus normality test and Brown–Forsythe tests respectively. When normality and equal variance between sample groups was achieved, one-way ANOVAs (followed by Bonferroni's multiple comparisons test), or t test were used. Where normality or equal variance of samples failed, Mann-Whitney U test were performed. Linear regression test, Chi-square test was used inappropriate situations. The sample sizes, specific statistical tests used, and the main effects of our statistical analyses for each experiment are reported in Supplementary Table 1.

1 Henn, F. A. & Vollmayr, B. Stress models of depression: Forming genetically vulnerable strains. *Neurosci Biobehav R* **29**, 799-804, (2005).

2 Li, K. *et al.* beta CaMKII in Lateral Habenula Mediates Core Symptoms of Depression. *Science* **341**, 1016-1020, (2013).

3 Powell, T. R., Fernandes, C. & Schalkwyk, L. C. in *Current Protocols in Mouse Biology* (John Wiley & Sons, Inc., 2011).

References

1 Halassa, M. M. & Haydon, P. G. Integrated Brain Circuits: Astrocytic Networks Modulate Neuronal Activity and Behavior. *Annu Rev Physiol* **72**, 335-355, (2010).

2 Giaume, C., Koulakoff, A., Roux, L., Holcman, D. & Rouach, N. NEURON-GLIA INTERACTIONS Astroglial networks: a step further in neuroglial and gliovascular interactions. *Nat Rev Neurosci* **11**, 87-99, (2010).

3 Khakh, B. S. & Sofroniew, M. V. Diversity of astrocyte functions and phenotypes in neural circuits. *Nat Neurosci* **18**, 942-952, (2015).

4 Attwell, D. *et al.* Glial and neuronal control of brain blood flow. *Nature* **468**, 232-243, (2010).

5 Volterra, A. & Meldolesi, J. Astrocytes, from brain glue to communication elements: The revolution continues. *Nat Rev Neurosci* **6**, 626-640, (2005).

6 Woo, D. H. *et al.* TREK-1 and Best1 Channels Mediate Fast and Slow Glutamate Release in Astrocytes upon GPCR Activation. *Cell* **151**, 25-40, (2012).

7 Molofsky, A. V. *et al.* Astrocytes and disease: a neurodevelopmental perspective. *Gene Dev* **26**, 891-907, (2012).

8 Araque, A., Parpura, V., Sanzgiri, R. P. & Haydon, P. G. Tripartite synapses: glia, the unacknowledged partner. *Trends Neurosci* **22**, 208-215, (1999).

9 Harada, Y. *et al.* Expressional analysis of inwardly rectifying Kir4.1 channels in Noda epileptic rat (NER). *Brain Res* **1517**, 141-149, (2013).

10 Neusch, C. *et al.* Lack of the kir4.1 channel subunit abolishes K+ buffering properties of Astrocytes in the ventral respiratory group: Impact on extracellular K+ regulation (vol 95, pg 1843, 2006). *J Neurophysiol* **96**, 965-965, (2006).

11 Li, K. *et al.* beta CaMKII in Lateral Habenula Mediates Core Symptoms of Depression. *Science* **341**, 1016-1020, (2013).

12 Proulx, C. D., Hikosaka, O. & Malinow, R. Reward processing by the lateral habenula in normal and depressive behaviors. *Nat Neurosci* **17**, 1146-1152, (2014).

13 Li, B. *et al.* Synaptic potentiation onto habenula neurons in the learned helplessness model of depression. *Nature* **470**, 535-539, (2011).

14 Matsumoto, M. & Hikosaka, O. Lateral habenula as a source of negative reward signals in dopamine neurons. *Nature* **447**, 1111-U1111, (2007).

15 Shabel, S. J., Proulx, C. D., Trias, A., Murphy, R. T. & Malinow, R. Input to the Lateral Habenula from the Basal Ganglia Is Excitatory, Aversive, and Suppressed by Serotonin. *Neuron* **74**, 475-481, (2012).

16 Stamatakis, A. M. & Stuber, G. D. Activation of lateral habenula inputs to the ventral midbrain promotes behavioral avoidance. *Nat Neurosci* **15**, 1105-+, (2012).

17 Lammel, S. *et al.* Input-specific control of reward and aversion in the ventral tegmental area. *Nature* **491**, 212-+, (2012).

18 Sartorius, A. *et al.* Remission of Major Depression Under Deep Brain Stimulation of the Lateral Habenula in a Therapy-Refractory Patient. *Biol Psychiat* **67**, E9-E11, (2010).

19 Lecca, S. *et al.* Rescue of GABA(B) and GIRK function in the lateral habenula by protein phosphatase 2A inhibition ameliorates depression-like phenotypes in mice. *Nat Med* **22**, 254-261, (2016).

20 Shabel, S. J., Proulx, C. D., Piriz, J. & Malinow, R. GABA/glutamate co-release controls habenula output and is modified by antidepressant treatment. *Science* **345**, 1494-1498, (2014).
21 Cui, W. *et al.* Glial Dysfunction in the Mouse Habenula Causes Depressive-Like Behaviors and Sleep Disturbance. *Journal Of Neuroscience* **34**, 16273-16285, (2014).
22 Henn, F. A. & Vollmayr, B. Stress models of depression: Forming genetically vulnerable strains. *Neurosci Biobehav R* **29**, 799-804, (2005).
23 Adzic, M. *et al.* The contribution of hypothalamic neuroendocrine, neuroplastic and neuroinflammatory processes to lipopolysaccharide-induced depressive-like behaviour in female and male rats: Involvement of glucocorticoid receptor and C/EBP-beta. *Behavioural brain research* **291**, 130-139, (2015).
24 Olsen, M. L. & Sontheimer, H. Functional implications for Kir4.1 channels in glial biology: from K+ buffering to cell differentiation. *J Neurochem* **107**, 589-601, (2008).
25 Djukic, B., Casper, K. B., Philpot, B. D., Chin, L. S. & McCarthy, K. D. Conditional knock-out of Kir4.1 leads to glial membrane depolarization, inhibition of potassium and glutamate uptake, and enhanced short-term synaptic potentiation. *The Journal of neuroscience : the official journal of the Society for Neuroscience* **27**, 11354-11365, (2007).
26 Tong, X. P. *et al.* Astrocyte Kir4.1 ion channel deficits contribute to neuronal dysfunction in Huntington's disease model mice. *Nat Neurosci* **17**, 694-703, (2014).
27 Kettenmann, H., Kettenmann, H. & Ransom, B. R. *Neuroglia*. 3rd edn, (Oxford University Press, 2013).
28 Ransom, C. B. & Sontheimer, H. Biophysical And Pharmacological Characterization Of Inwardly Rectifying K+ Currents In Rat Spinal-Cord Astrocytes. *J Neurophysiol* **73**, 333-346, (1995).
29 Newman, E. & Reichenbach, A. The Muller cell: A functional element of the retina. *Trends Neurosci* **19**, 307-312, (1996).
30 Amedee, T., Robert, A. & Coles, J. A. Potassium homeostasis and glial energy metabolism. *Glia* **21**, 46-55, (1997).
31 Neusch, C. *et al.* Lack of the Kir4.1 channel subunit abolishes K+ buffering properties of astrocytes in the ventral respiratory group: impact on extracellular K+ regulation. *J Neurophysiol* **95**, 1843-1852, (2006).
32 Newman, E. A. Inward-Rectifying Potassium Channels In Retinal Glial (Muller) Cells. *Journal Of Neuroscience* **13**, 3333-3345, (1993).
33 Rojas, L. & Orkand, R. K. K+ channel density increases selectively in the endfoot of retinal glial cells during development of Rana catesbiana. *Glia* **25**, 199-203, (1999).
34 Li, L., Head, V. & Timpe, L. C. Identification of an inward rectifier potassium channel gene expressed in mouse cortical astrocytes. *Glia* **33**, 57-71, (2001).
35 Shigetomi, E. *et al.* Imaging calcium microdomains within entire astrocyte territories and endfeet with GCaMPs expressed using adeno-associated viruses. *J Gen Physiol* **141**, 633-647, (2013).
36 Hibino, H. *et al.* Inwardly Rectifying Potassium Channels: Their Structure, Function, and Physiological Roles. *Physiol Rev* **90**, 291-366, (2010).

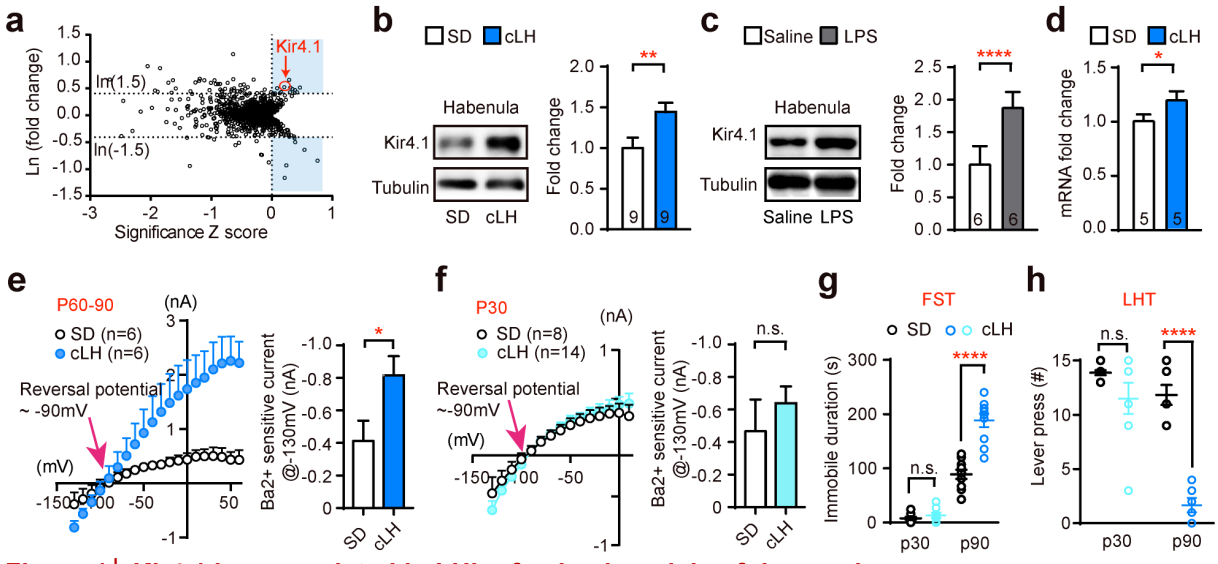

Figure 1 | Kir4.1 is upregulated in LHb of animal models of depression.

a, Volcano plot of high-throughput proteomic screen identifies differentially expressed proteins in habenula of cLH rats. Ln (fold change) was Ln transformed value of the normalized protein ratio of cLH and control. Significance Z score was calculated as the average normalized ratio minus two folds of standard deviation. Proteins in the shaded areas have more than 50% significant change[11]. Kir4.1 is one of the eight upregulated proteins identified. Dash lines indicate fold change of 50%.

b, **c**, Western blot analysis showing upregulation of Kir4.1 protein in membrane fraction of habenula of cLH (**b**) and LPS-induced depression rat models (**c**). Tubulin is used as loading control. Numbers in the bars indicate the number of animals used.

d, QPCR analysis of Kir4.1 mRNA in habenula.

e, **f**, I-V plot and bar graph showing Ba^{2+}-sensitive current in cLH rats and their wild type controls at the age of P60-90 (**e**) and P30 (**f**).

g, **h**, Age-dependent forced swim (FST, **g**) and learned helpless (LHT, **h**) phenotypes of cLH rats. Low number of lever press and high immobility time indicate depressive-like phenotype in P90 cLH rats.

Data are means ± SEM. *P < 0.05, **P <0.01, ****P < 0.0001; n.s., not significant (See Supplementary Table 1 for statistical analysis and n numbers).

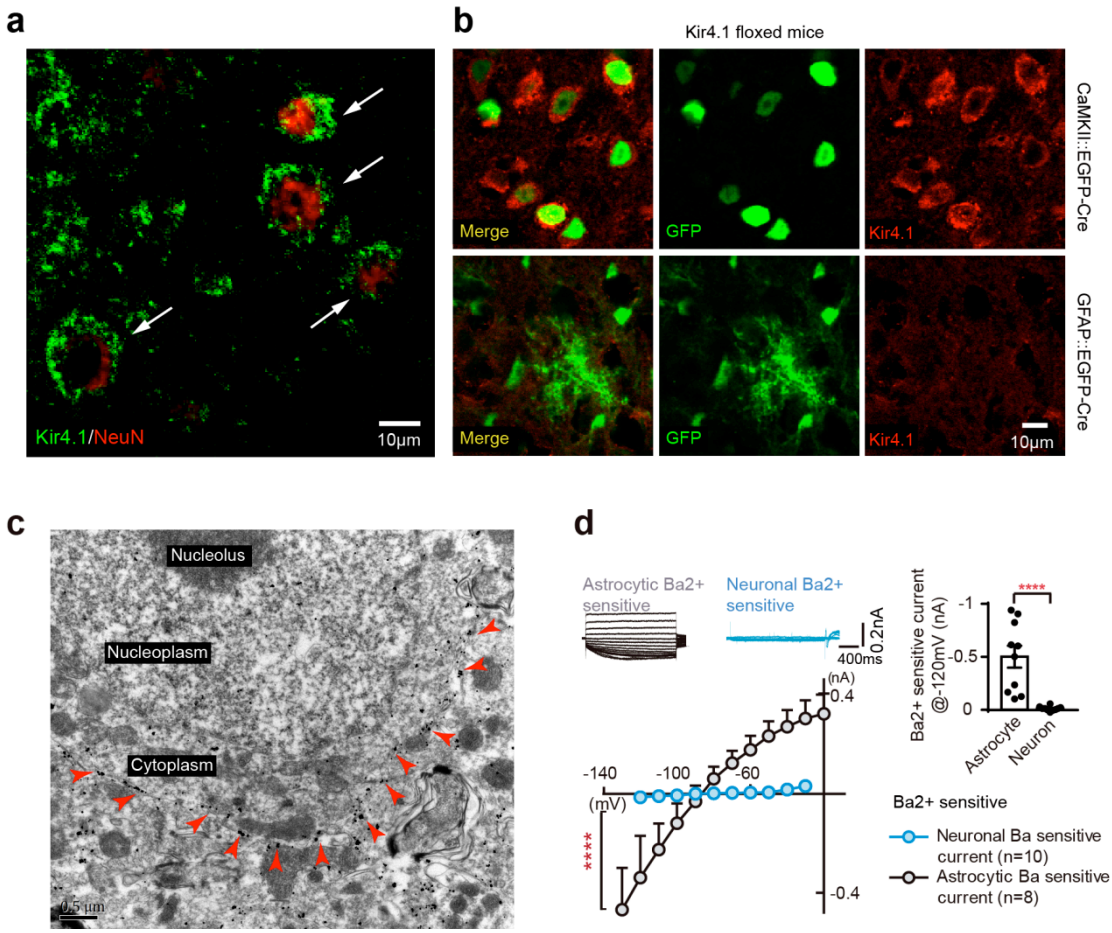

Figure 2 | Kir4.1 is expressed on astrocytic processes tightly wrapping around neuronal soma in LHb.

a, Immunohistochemistry signals of Kir4.1 envelope neuronal soma as indicated by white arrows.

b, The pan-soma Kir4.1 signals remain intact in LHb of Kir4.1$^{f/f}$ floxed mice injected with AAV2/1-CaMKII::EGFP-Cre, but are eliminated when injected with AAV2/5-GFAP::EGFP-Cre (GFAP: human astrocyte-specific GFAP promoter, gfaABC1D).

c, Immunogold electron microscopy of Kir4.1. Red arrows indicate gold signals surrounding a neuronal soma.

d, I-V plots of the Ba^{2+} sensitive Kir4.1 current recorded in LHb astrocytes and neurons, with representative traces shown in up-left and statistic bar graph of current recorded when cells are held at -120mV shown in up-right.

Data are means ± SEM. ****P < 0.0001 (See Supplementary Table 1 for statistical analysis and n numbers).

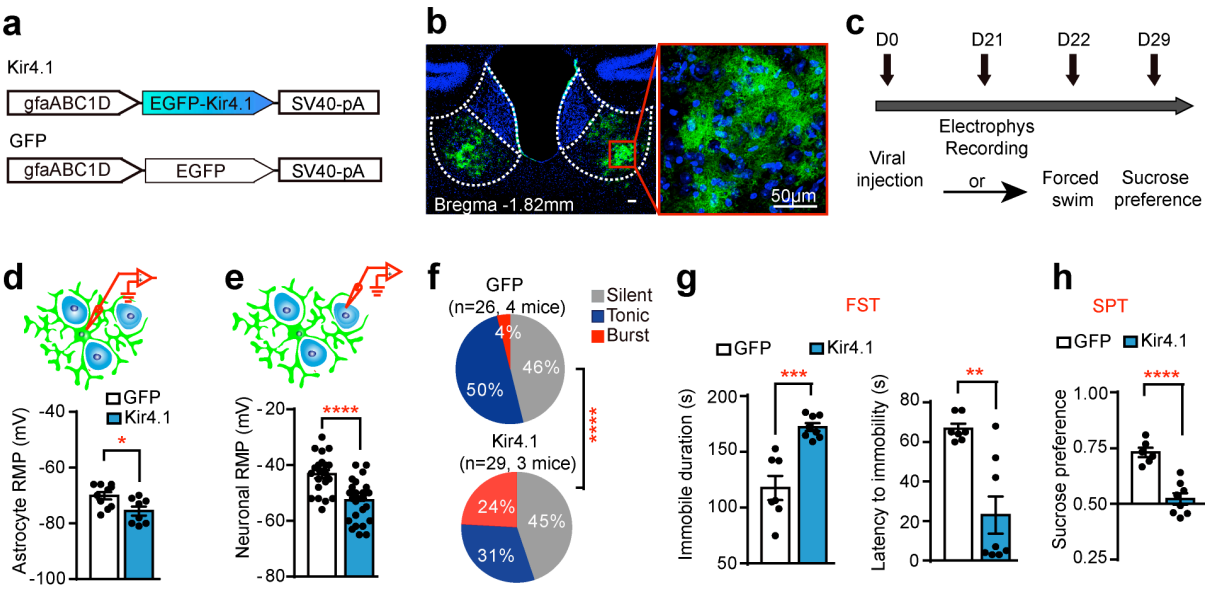

Figure 3| Astrocytic kir4.1 overexpression increases neuronal bursts in LHb and causes depressive-like phenotypes.

a, Schematics of AAV vectors engineered to overexpress Kir4.1 or a GFP control and under a GFAP promoter.

b, Illustration of bilateral viral injection of AAV-GFAP::Kir4.1 in mouse LHb (stained with antibody against GFP and Hoechst).

c, Experimental paradigm for electrophysiology and behavioral testing.

d-**f**, Astrocytic overexpression of Kir4.1 decreases RMPs of both astrocytes (**d**) and neurons (**e**) and increases the bursting population in neurons (**f**).

g, **h**, Behavioral effects of expressing various viral constructs in LHb in forced swim test (FST) (**h**) and sucrose preference test (SPT) (**i**).

Data are means ± SEM. *P <0.05, **P <0.01, ***P < 0.001, ****P< 0.0001 (See Supplementary Table 1 for statistical analysis and n numbers).

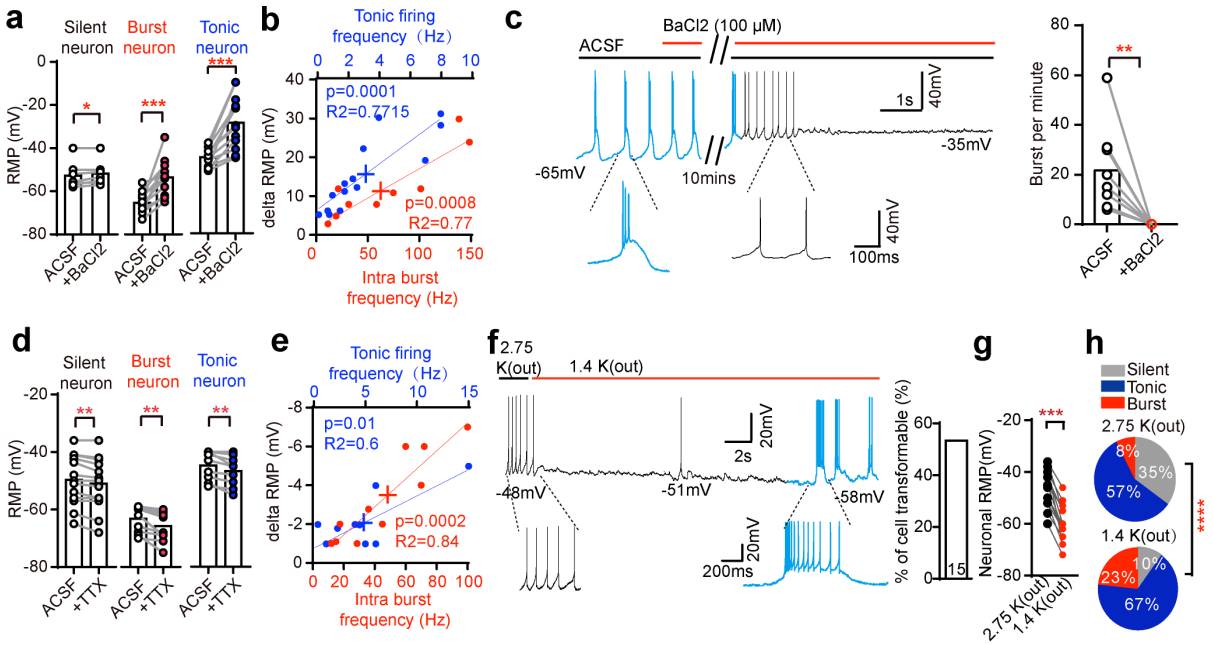

Figure 4 | Kir4.1-dependent potassium buffering regulates neuronal RMP and bursting in LHb.

a, **d**, Changes of neuronal RMPs caused by $BaCl_2$ (100 μM, **a**) or TTX (1μM, **d**) in different neuronal types. RMPs are measured at 15min or 5min after perfusion of $BaCl_2$ or TTX, respectively, when the RMPs stabilize.

b, **e**, Changes of neuronal RMPs after $BaCl_2$ (**b**) or TTX (**e**) treatments correlate with original firing rates of tonic-firing neurons (blue) or intra-burst frequencies of bursting neurons (red).

c, Representative trace (left) and bar graph (right) showing $BaCl_2$ effect (sampled at 15mins after drug perfusion) onto bursting neurons. Spikes in bursting mode are marked in blue. Spikes in tonic-firing mode are marked in black.

f, Example (left) and percentage of LHb neurons transforming from tonic- to burst- firing mode after Kout is switched from normal (2.75 mM) to half (1.4mM) (sampled at 1min after drug perfusion).

g, **h**, Lowering Kout to half decreases neuronal RMPs (**g**) and increases bursting neural population (**h**).

Data are means ± SEM. *P < 0.05, **P < 0.01, ***P < 0.001, ****P < 0.0001, n.s., not significant (See Supplementary Table 1 for statistical analysis and n numbers).

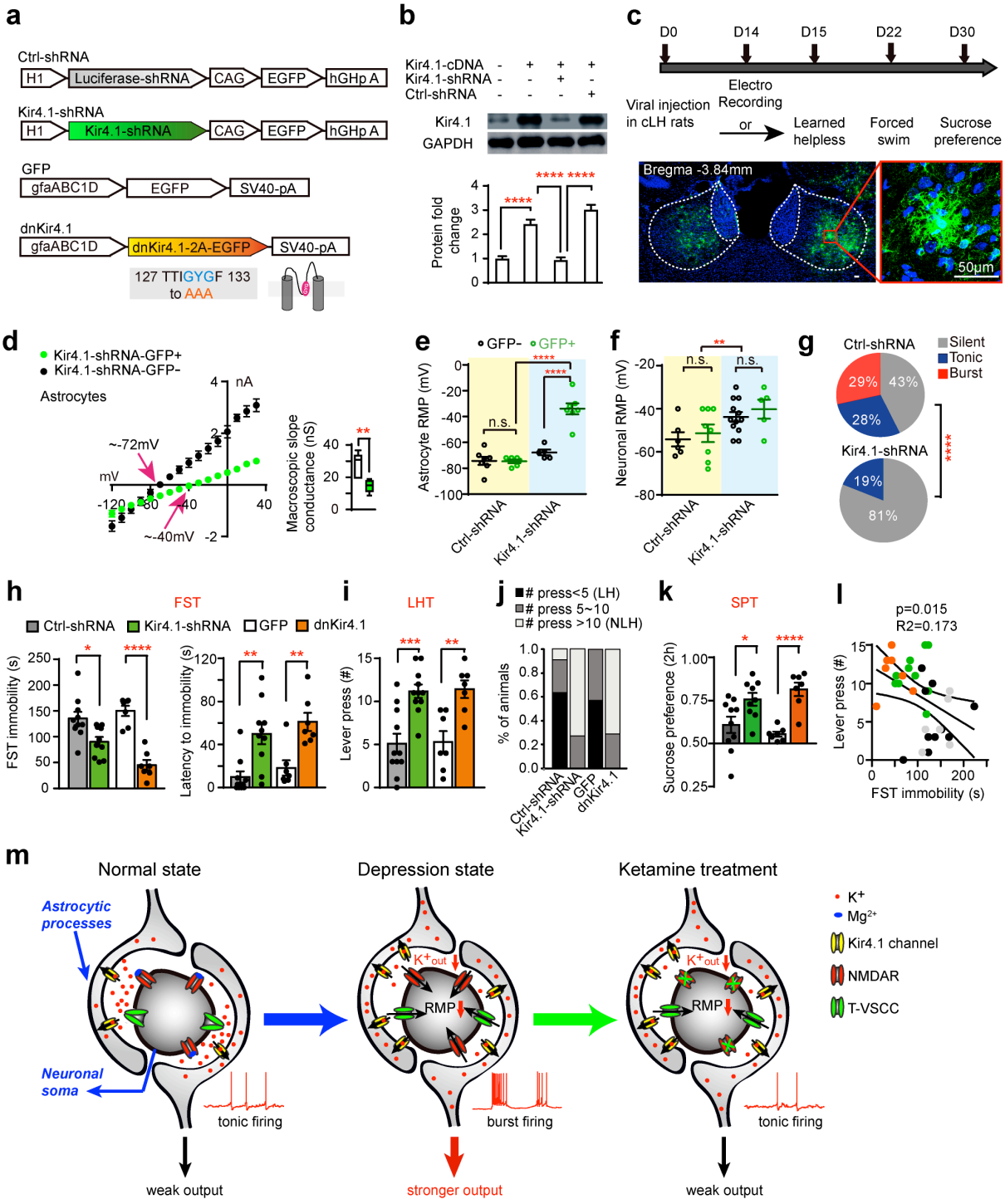

Figure 5| Loss of function of Kir4.1 in LHb decreases neuronal bursting and rescues depressive-like phenotypes of cLH rats.

a, Schematics of the AAV vector engineered to overexpress shRNA or dominant negative form of Kir4.1. H1: human H1 promoter. CAG: The CMV early enhancer/chicken beta actin promoter. Three point mutations in the dnKir4.1 and their locations are indicated.

b, Western blot and quantification showing efficient knock-down of Kir4.1 by shRNA in HEK293T cells.

c, Experimental paradigm for behavioral testing of cLH rats infected by virus (top) and illustration of bilateral expression of AAV-GFAP::dnKir4.1 in LHb (stained with antibody against GFP and Hoechst).

d-**g**, AAV-Kir4.1-shRNA caused a shift of reverse potential from -72mV to -40mV in astrocytes (**d**), depolarization of astrocytes (**e**) and neurons in viral infected region (**f**), and abolished neuronal bursting (**g**). Floating bars for membrane slope conductance in **d** is calculated from the I/V plots (between −120 and +40 mV).

h-**k**, Behavioral effects of expressing various viral constructs in the LHb of cLH rats in FST (**h**), LHT (**i**, **j**) and SPT (**k**). **j**: Percentage of rats in each category. LH: learned helpless rats with <5 lever presses; NLH, non–learned helpless rats with >10 lever presses.
l, FST immobility is highly correlated with learned helpless phenotype.
m, A model for mechanisms of depression and ketamine treatment at LHb. Upregulation of Kir4.1 on astrocytic processes surrounding neuronal soma leads to enhanced K+ buffering at the tight neuron-glia junction, decreased Kout and hyperpolarized neuronal RMP. Consequently, de-inactivation of T-VSCCs initiates NMDAR-dependent bursts, causing a stronger output of LHb to trigger depression. Ketamine blockade of NMDARs stops bursts and relieves depression.
Data are means ± SEM.*P < 0.05, **P < 0.01, ***P < 0.001, ****P< 0.0001, n.s., not significant (See Supplementary Table 1 for statistical analysis and n numbers).

Extended data

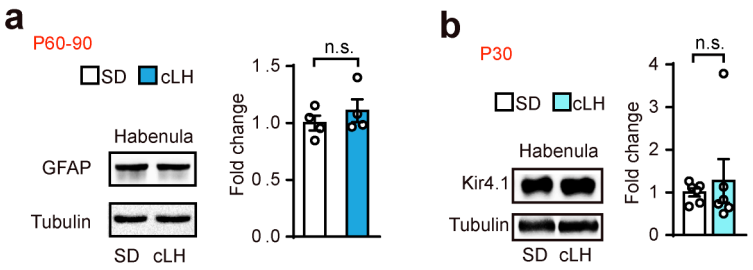

Extended Data Figure 1 | Kir4.1 is unchanged in p30 cLH rats.

a, Western blot analysis showing no change of GFAP protein in habenula of cLH rats at the age of P60-90.

b, Western blot analysis showing no change of Kir4.1 protein in membrane fraction of habenula in cLH rats at the age of P30.

Data are means ± SEM. n.s., not significant (See Supplementary Table 1 for statistical analysis and n numbers).

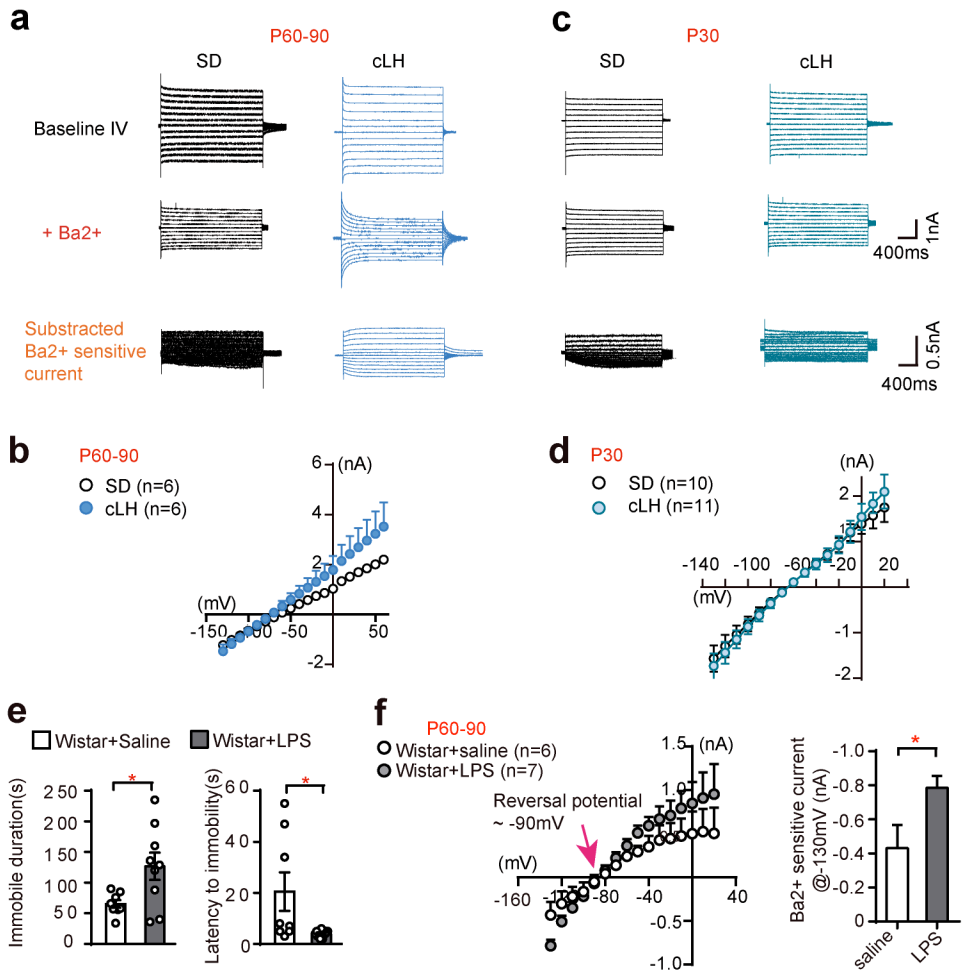

Extended Data Figure 2 | Ba-sensitive Kir4.1 current is upregulated in LHb of adult cLH and LPS-induced depressive-like animals.

a, c, Representative traces showing linear I-V curve in a typical astrocyte before (upper) and after (middle) Ba^{2+} perfusion under voltage steps (-130mV to -30 mV, step by 10mV, 2s duration, holding at -70mV). Subtraction of the two led to Ba-sensitive Kir current (bottom) in P60-90 (**a**) and P30 (c) cLH rats.

b, d, I-V plot of astrocytes in cLH rats and SD controls at the age of P60-90 (**b**) and P30 (**d**).

e, LPS injection (500 μg/kg, i.p., for 7 days) induces increased immobile time and decreased latency to immobility in FST.

f, I-V plot and bar graph showing Ba^{2+}-sensitive current in LPS injected Wistar rats and their saline controls at the age of P60-90.

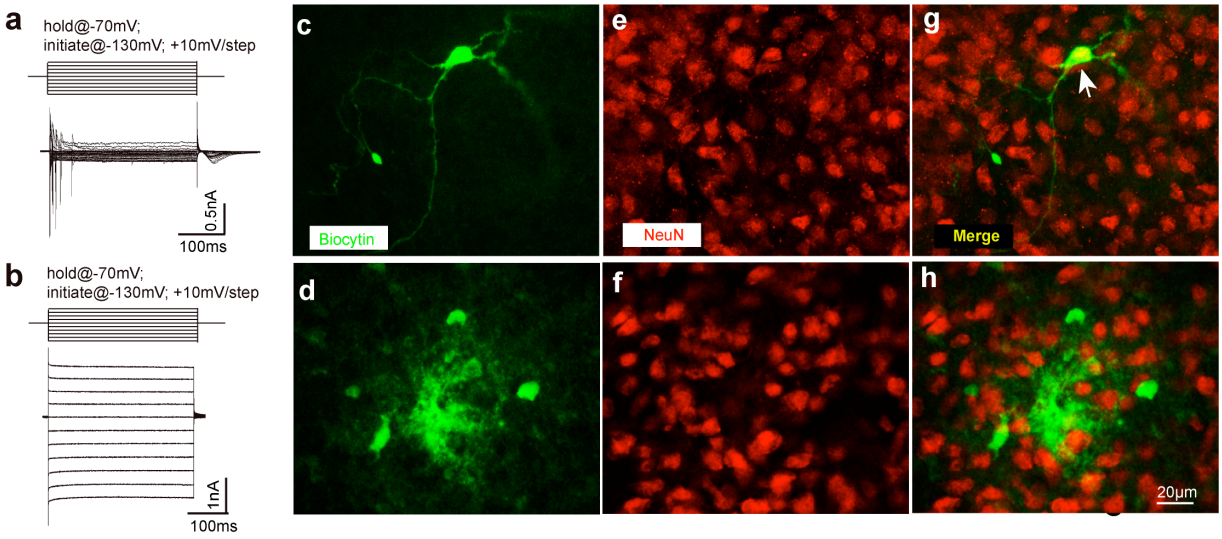

Extended Data Figure 3 | Biocytin intercellular filling and double staining with NeuN confirm the identity of eletrophysiologically identified neurons and astrocytes.

a, **b**, A neuron (**a**) and an astrocyte (**b**) in LHb slices are first identified based on their specific morphology (astrocytes: 5-10μm diameter; neuron: ~15μm diameter) and physiological properties. The neuron fires at a depolarizing voltage step (**a**), whereas the astrocyte shows a steady-state I–V relationship and a lack of spiking activity (**b**). After electrophysiological characterization, cells are held for at least 30 minutes in voltage clamp and constantly injected with a hyperpolarization current (500ms, 50pA, 0.5Hz, 30min) to allow biocytin filling.

c-**h**, Biocytin labeled neurons and astrocytes subsequently confirmed by co-labeling with NeuN.

c, **d**, Biocytin signals in a single neuron (**c**) or a group of astrocytes due to diffusion through gap junctions (**d**).

e, **f**, NeuN signals.

g, **h**, Colabeling of NeuN with the neuron (indicated by white arrow, **g**) but not astrocytes (**h**). Note that all biocytin filled neurons (n = 18) show colabel with NeuN and all biocytin filled astrocytes (n = 11) do not colabel with NeuN.

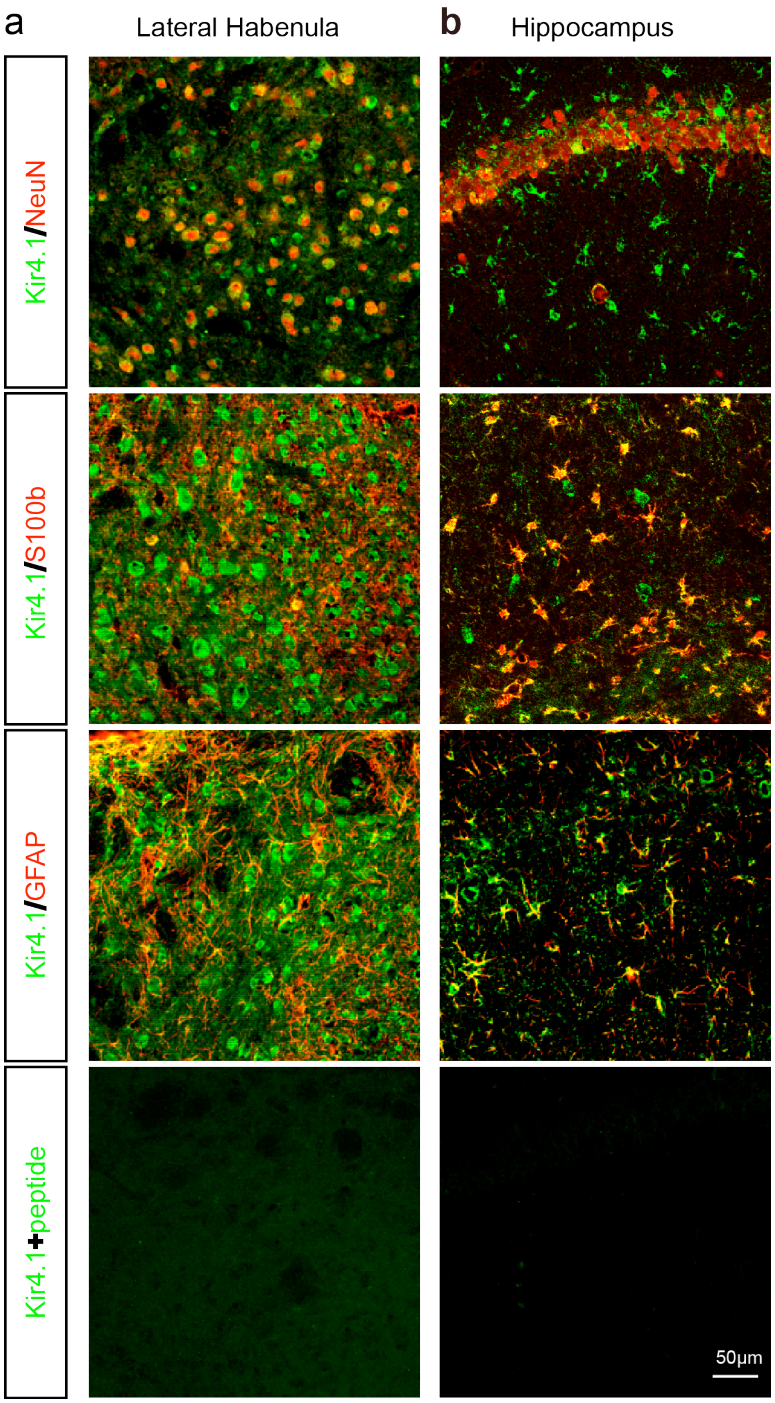

Extended Data Figure 4 | Expression pattern of Kir4.1 in LHb and hippocampus.
a, b, Kir4.1 co-immunostaining with neuronal marker (NeuN) or astrocytic marker (S100b and GFAP) in LHb (**a**) or hippocampus (**b**). Bottom two panels are staining with the same kir4.1 antibody pre-incubated with the antigen peptide, demonstrating the specificity of Kir4.1 antibody.

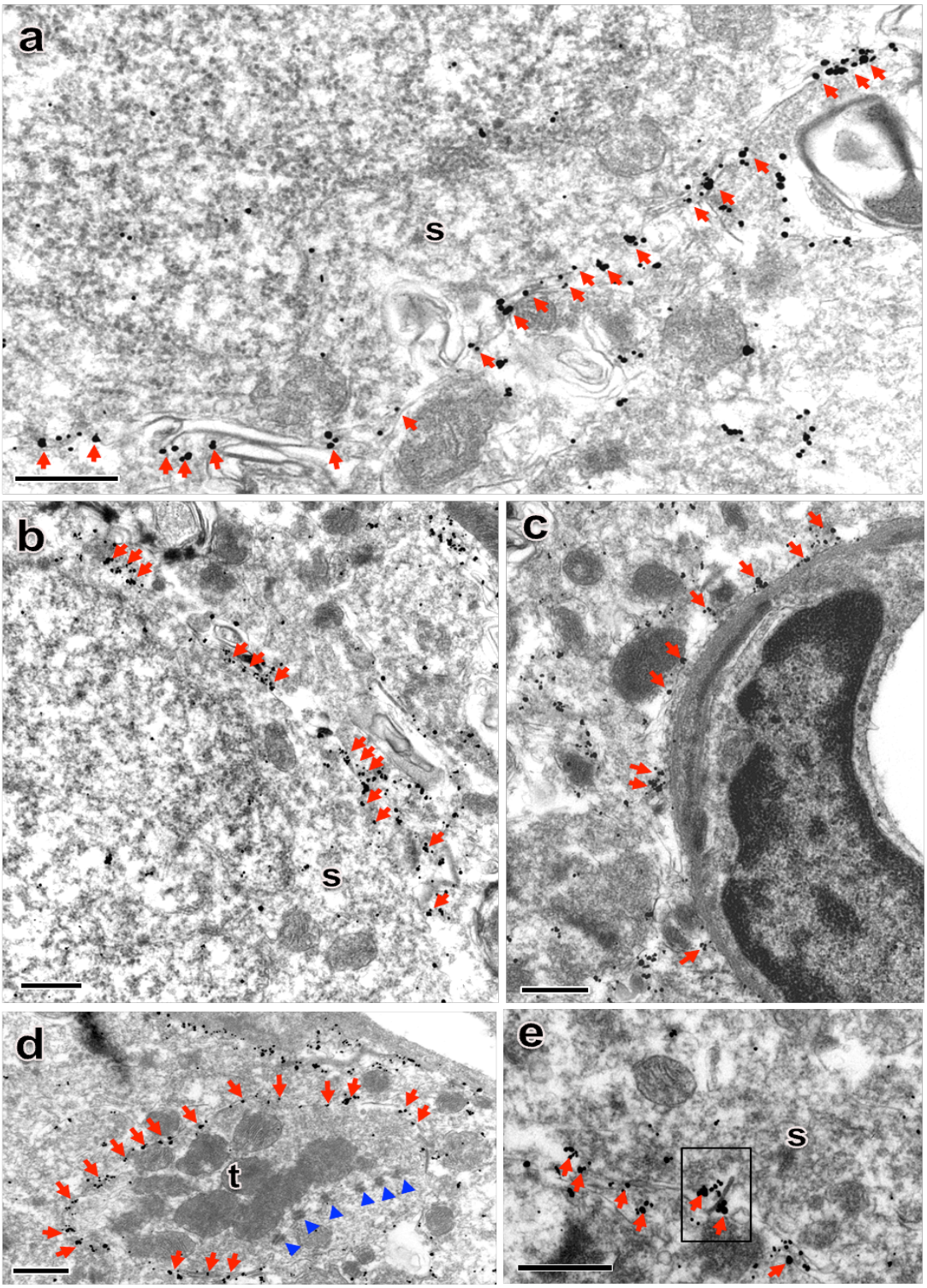

Extended Data Figure 5 | Electron microscopy immunohistochemistry of Kir4.1 staining.

a-c, Many Kir4.1 immunograins (arrows) surround the neuronal soma (**a**, **b**) and the vascular endothelial cell (**c**).

d, The Kir4.1 grains (arrows) also surround the axon-dendritic synapses, but are rare near the synaptic zones as indicated by the postsynaptic densities (arrowheads).

e, Insert shows Kir4.1 immunograins near a gap junction.

s: neuronal soma; t: axon terminal. Scale bars= 0.5 um.

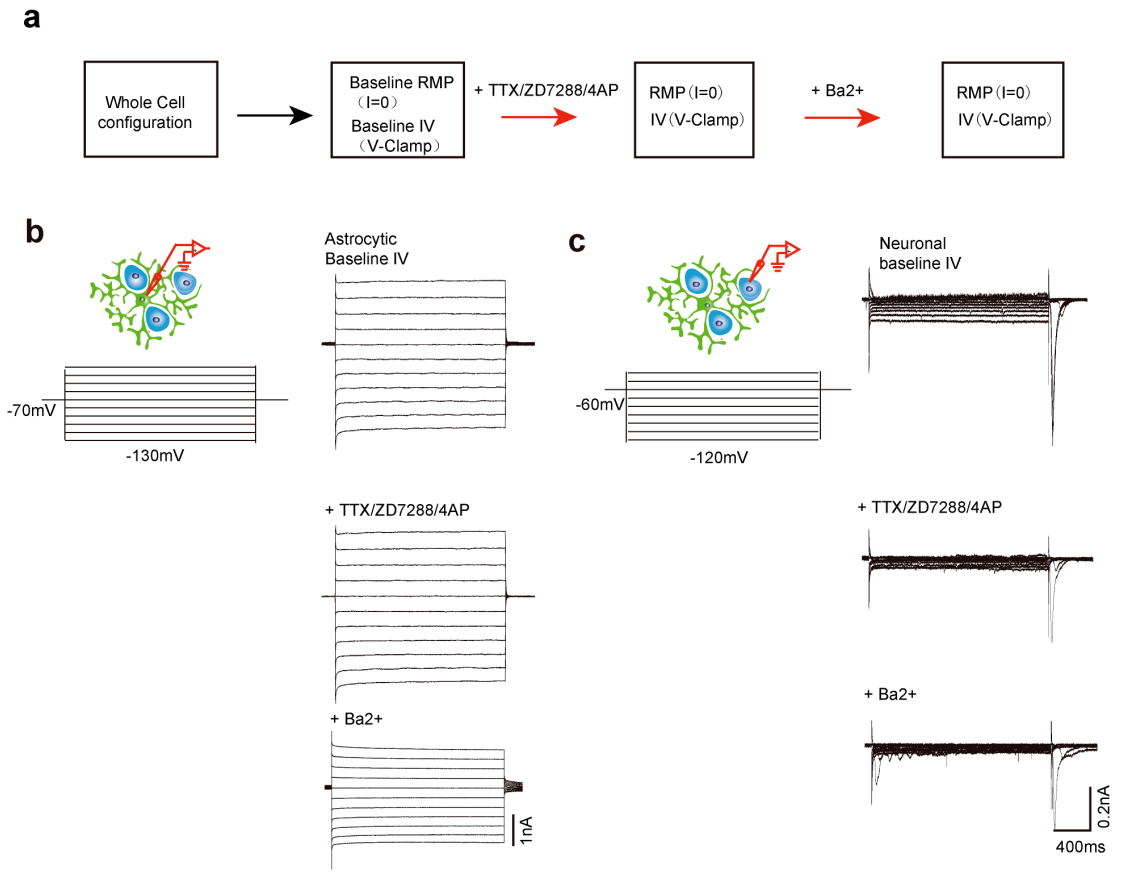

Extended Data Figure 6 | Kir4.1 is expressed in astrocytes but not neurons in LHb.

a, Schematics showing sequence of drug application and recording after a neuron or astrocyte is patched.

b, Representative traces showing a linear I-V curve in a typical astrocyte under voltage steps (-130mV to -30 mV, step by 10mV, 2s duration, holding at -70mV, protocol demonstrated on left) (upper panel). I-V curves of the same cell after addition of TTX (1uM), ZD7288 (50uM) and 4AP (1mM, middle), and further addition of Ba^{2+} (100uM, bottom) are shown below.

c, Representative traces showing a non-linear I-V curve in a typical neuron under voltage steps (-130mV to -30 mV, step by 10mV, 2s duration, holding at -70mV, protocol demonstrated on left) (upper panel). I-V curves of the same cell after addition of TTX, ZD7288 and 4AP (middle), and further addition of Ba^{2+} (bottom) are shown below.

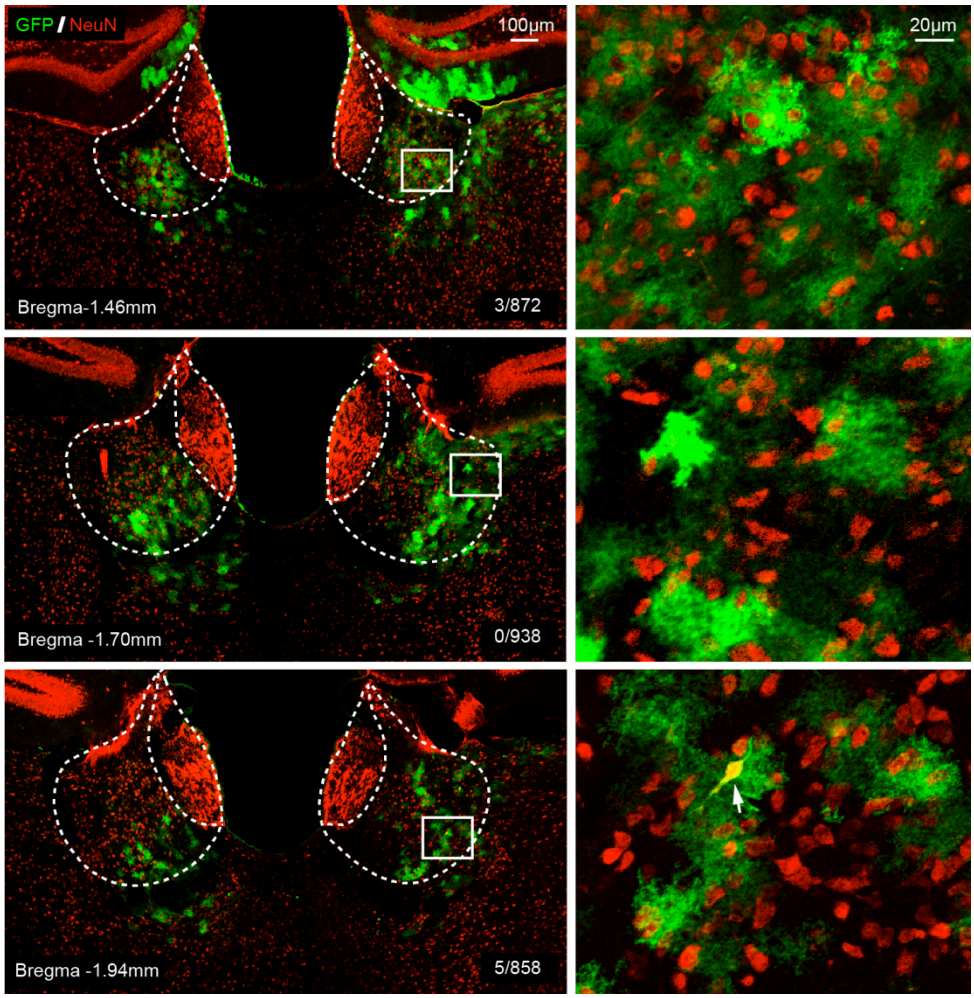

Extended Data Figure 7 | Characterization of cell-type specificity of GFAP promoter driven expression of Kir4.1 in mouse LHb

Double immunofluorescence for mouse NeuN (red) and GFP (green) in the coronal section of LHb brain slices infected with AAV-GFAP::Kir4.1 (AAV2/5-gfaABC1D-EGFP-Kir4.1) virus. Left are examples of anterior, middle and posterior coronal section of LHb. Numbers in the bottom right corner are the number of merged cells/ number of NeuN+ cells in the viral-infected area. Right are zoom-in images of the white square area in left. Note that there is only one infected neuron, as indicated by the white arrow, in all three fields of view.

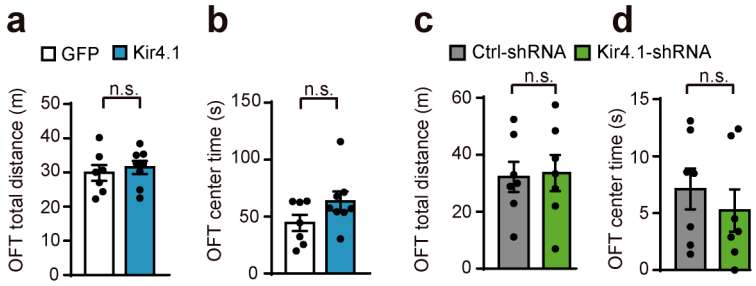

Extended Data Figure 8 | Overexpression of Kir4.1 or Kir4.1-shRNA in LHb does not affect locomotion in open field test.

a-b, Overexpression of Kir4.1 in LHb does not affect locomotion activities.

c-d, Overexpression of Kir4.1-shRNA in LHb does not affect locomotion activities.

Data are means ± SEM. n.s., not significant (See Supplementary Table 1 for statistical analysis and n numbers).

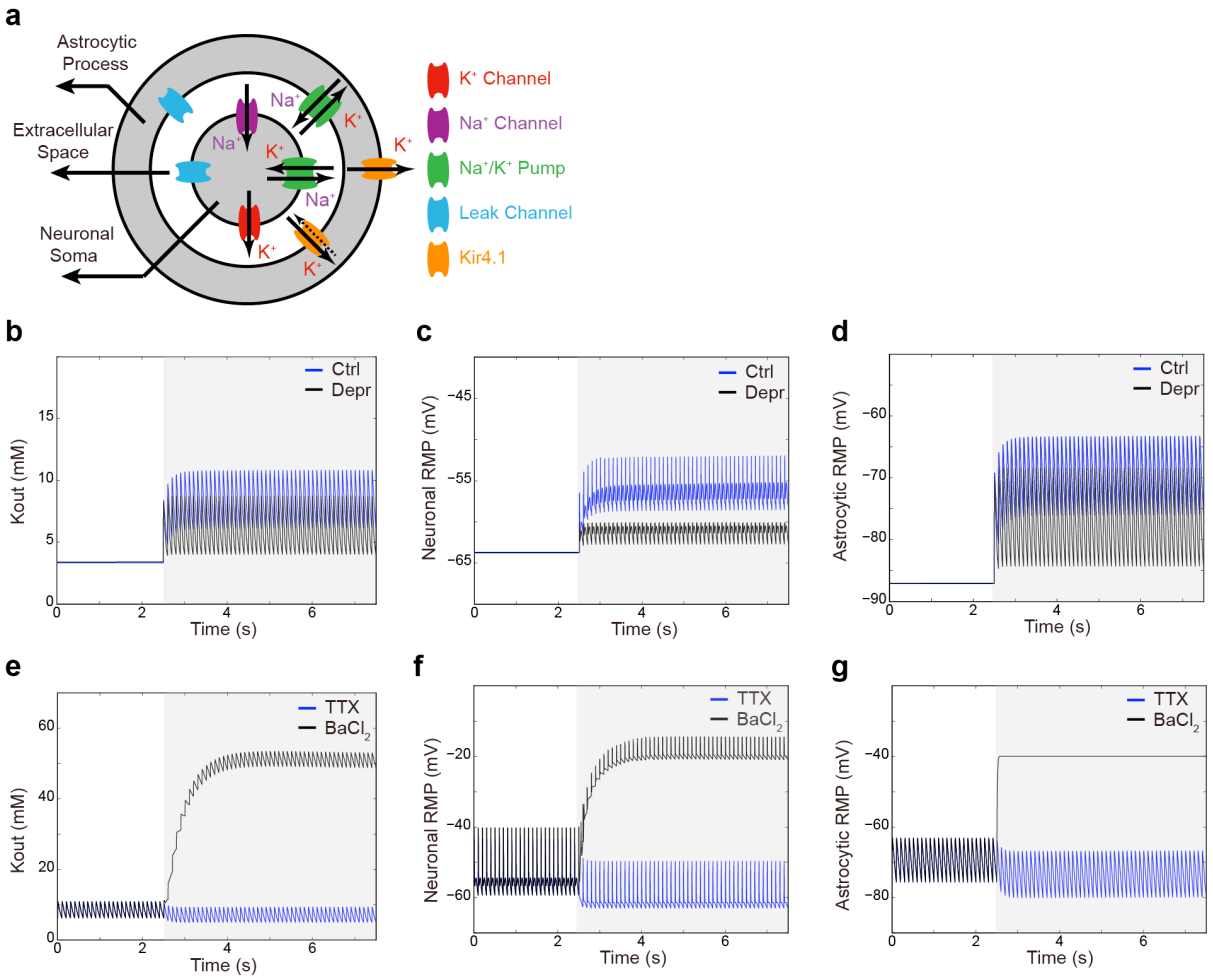

Extended Data Figure 9 | Simulation of the dynamic potassium buffering effect of Kir4.1 in the tri-compartment model.

a, Schematic representation of a tri-compartment model involving neuron, astrocyte and extracellular space in between.

b-d, Effects of increasing Kir4.1 expression level on extracellular K^+ concentration (**b**), neuronal membrane potential (**c**) and astrocytic membrane potential (**d**). Ctrl: control condition with 1x Kir4.1 conductance; Depr: depression condition with 2x Kir4.1 conductance. Grey shaded areas indicate application of 10 Hz tonic stimulation to neurons. Note that under this neuronal firing condition, Kout is lower, and neuron and astrocyte are more hyperpolarized in Depr than in Ctrl.

e-g, Effects of *in silico* TTX (blocking APs, gNa = 0) or Ba^{2+} (blocking Kir4.1, gKir4.1=0) treatments on extracellular K^+ concentration (**e**), neuronal membrane potential (**f**) and astrocytic membrane potential (**g**) when neurons are under 10 Hz tonic stimulation. Grey shaded areas indicate *in silico* application of drugs. Note that TTX and Ba^{2+} cause opposite changes to Kout, neuronal membrane potential and astrocytic membrane potential.

Neuronal spikes are not shown for clarity of presentation.

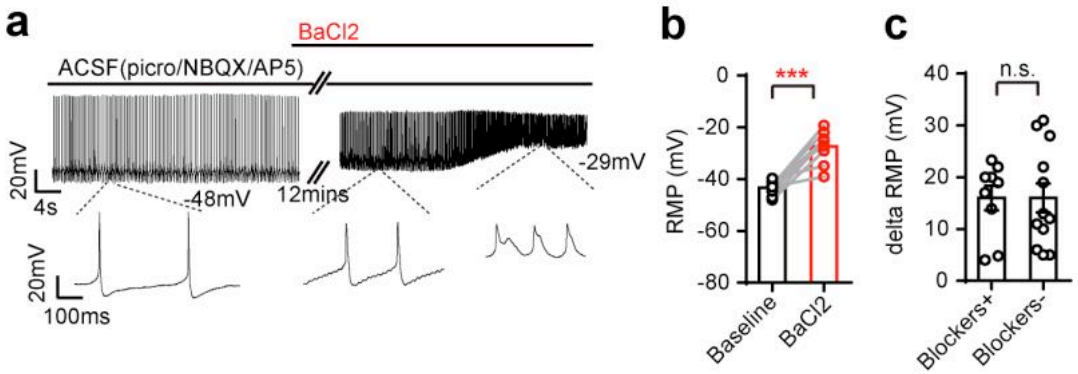

Extended Data Figure 10 | $BaCl_2$ caused depolarization of neuronal RMP in presence of synaptic transmitter blockers.

a, b, Representative trace (a) and bar graph (b) showing effect of $BaCl_2$ (100uM) perfusion onto tonic-firing neurons which have been bathed with transmitter blockers (100 uM picrotoxin, 10 uM NBQX and 100 uM AP5).

c, Bar graph showing the level of RMP depolarization caused by $BaCl_2$ in presence or absence of transmitter blockers.

Data are means ± SEM. ***P< 0.001, n.s., not significant (See Supplementary Table 1 for statistical analysis and n numbers)

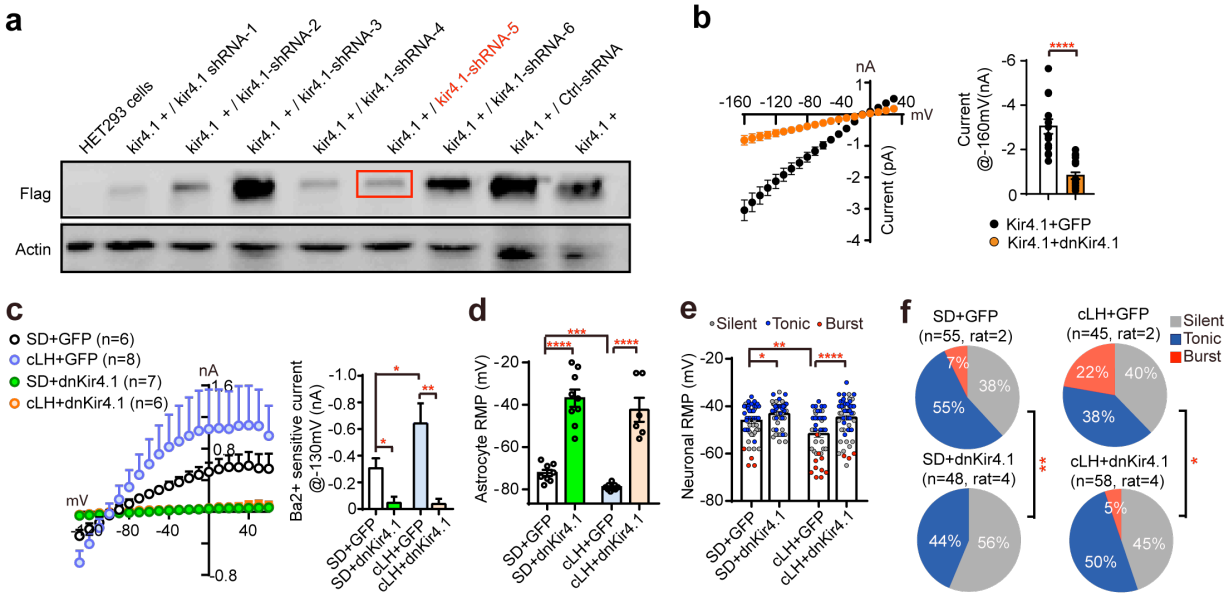

Extended Data Figure 11 | Characterization of Kir4.1 loss-of-function constructs.

a, Flag-tagged-Kir4.1 plasmid (pAAV-CMV-betaGlobin-Kir4.1-eGFP-3Flag) was co-transfected with pAAV-vector expressing 6 different shRNAs (see Methods) of Kir4.1 or the negative control (shRNA of luciferase) into HEK293TN cell. Based on the knock-down efficiency as shown in the western blot, Kir4.1-shRNA-5 was chosen for viral package.

b, I-V plot showing Kir4.1 currents recorded in HEK293 cells transfected with pAAV-Kir4.1 together with negative control pAAV-GFP or pAAV-dnKir4.1 plasmid. Bars represent the current values recorded at -160mV.

c, I-V plot and bar graph showing Ba2+-sensitive currents blocked by AAV-dnKir4.1 in both cLH and SD rats.

d-f, AAV-dnKir4.1 caused a depolarization of RMP in astrocytes (d) and neurons in viral infected area (e), and abolished neuronal bursting (f) in both cLH and SD rats.

Data are means ± SEM. *P < 0.05, **P < 0.01, ***P< 0.001, ****P< 0.0001 (See Supplementary Table 1 for statistical analysis and n numbers).

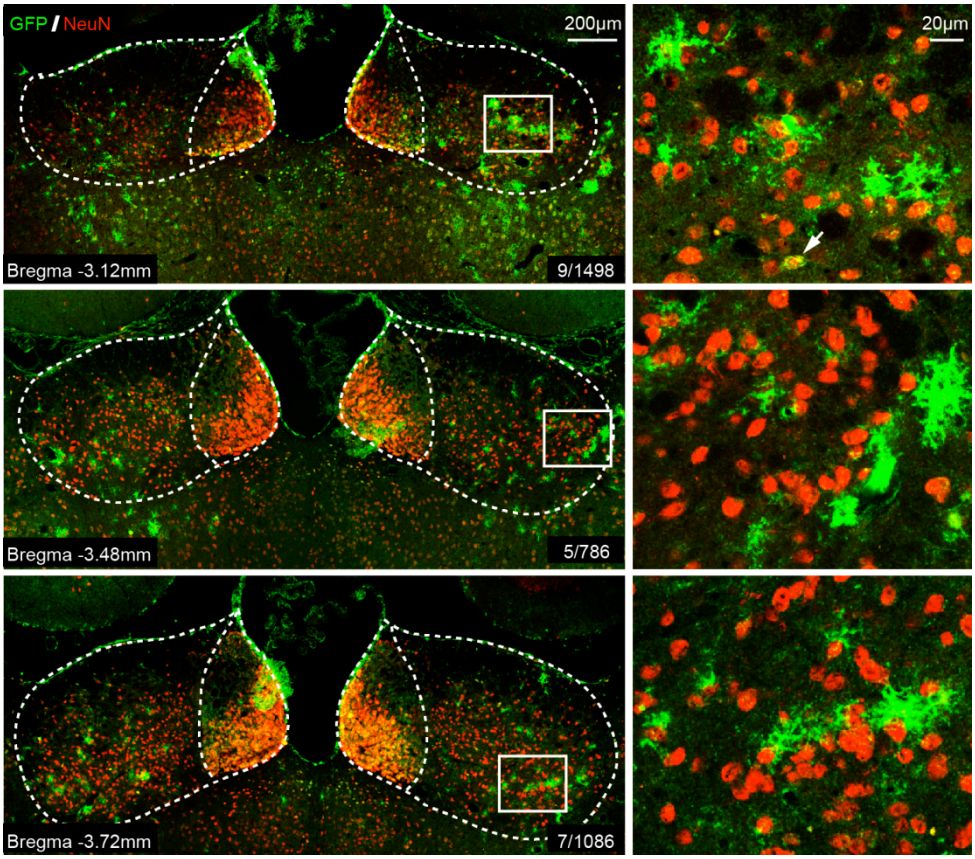

Extended Data Figure 12 | Characterization of cell-type specificity of GFAP promoter driven expression of dnKir4.1 in rat LHb.

Double immunofluorescence for rat NeuN (red) and GFP (green) in the coronal section of LHb brain slices infected with AAV-GFAP::dnKir4.1 (AAV2/5-gfaABC1D-dnKir4.1-2A-eGFP) virus. Left are examples of anterior, middle and posterior coronal section of LHb. Numbers in the bottom right corner are the number of merged cells/ number of NeuN+ cells in the viral-infected area. Right are zoom-in images of the white square area in left. Note that there is only one infected neuron, as indicated by the white arrow, in all three fields of view.

Contents

Supplementary Table 2: Model parameters

	Value	Unit	Parameter
R	8.31	$J \cdot mol^{-1} \cdot K^{-1}$	Gas constant
T	308	K	Absolute temperature
F	96485	$C \cdot mol^{-1}$	Faraday constant
$\mathbf{dt}$	0.1	ms	Step time
$\mathbf{c_N}$	30	pF	Neuronal capacitance
$\mathbf{c_A}$	1	pF	Astrocytic capacitance
$\mathbf{g_K}$	20	nS	Neuronal K^+ channel conductance
$\mathbf{g_{Na}}$	120	nS	Neuronal Na^+ channel conductance
$\mathbf{g_{Leak,N}}$	0.5	nS	Neuronal leak conductance
$\mathbf{V_{Leak,N}}$	−50	mV	Neuronal leak potential
$\mathbf{i_{max,N}}$	0.12	$mM \cdot ms^{-1}$	Neuronal Na^+/K^+ pump rate
$\mathbf{g_{Kir}}$	12	nS	Astrocytic Kir4.1 channel conductance on extracellular side
$\mathbf{g_{Kir\_vess}}$	12.5	nS	Astrocytic Kir4.1 channel conductance on vessel side
$\mathbf{g_{Leak,A}}$	0.1	nS	Astrocytic leak conductance
$\mathbf{V_{Leak,A}}$	−40	mV	Astrocytic leak potential
$\mathbf{i_{max,A}}$	0.12	$mM \cdot ms^{-1}$	Astrocytic Na^+/K^+ pump rate
$\mathbf{V_h}$	178.46	mV	Kir4.1 channel parameter
$\mathbf{V_s}$	119.47	mV	Kir4.1 channel parameter
$\mathbf{V_{rest\_A}}$	-10	mV	Kir4.1 channel parameter
$\mathbf{km_k}$	3.0	mM	Na^+/K^+ pump parameter
$\mathbf{km_{Na}}$	10.	mM	Na^+/K^+ pump parameter
$\mathbf{V_N}$	−63.76	mV	Initial neuronal membrane potential
$\mathbf{V_A}$	−87.08	mV	Initial astrocyte membrane potential
$\mathbf{[K^+]_N}$	135.04	mM	Initial neuronal K^+ concentration
$\mathbf{[K^+]_o}$	3.34	mM	Initial extracellular K^+ concentration
$\mathbf{[K^+]_A}$	135.00	mM	Initial astrocytic K^+ concentration
$\mathbf{[Na^+]_N}$	11.16	mM	Initial neuronal Na^+ concentration

$[\mathbf{Na^+}]_{\mathbf{o}}$	145.95	mM	Initial extracellular Na^+ concentration
$[\mathbf{Na^+}]_{\mathbf{A}}$	7.00	mM	Initial astrocytic Na^+ concentration
$\mathbf{Vol_o}$	0.01	pL	Extracellular volume
$\mathbf{Vol_N}$	1.08	pL	Neuronal volume
$\mathbf{Vol_A}$	1.08	pL	Astrocytic volume
$\mathbf{d_{K\_N}}$	0.0001	ms^{-1}	K^+ effective flux rate in the neuron
$\mathbf{d_{K\_O}}$	0.001	ms^{-1}	K^+ effective flux rate in the extracellular space
$\mathbf{d_{K\_A}}$	0.1	ms^{-1}	K^+ effective flux rate in the astrocyte
$\mathbf{d_{Na\_N}}$	0.0001	ms^{-1}	Na^+ effective flux rate in the neuron
$\mathbf{d_{Na\_O}}$	0.01	ms^{-1}	Na^+ effective flux rate in the extracellular space
$\mathbf{d_{Na\_A}}$	0.01	ms^{-1}	Na^+ effective flux rate in the astrocyte
$[\mathbf{K^+}]_{\mathbf{N\_0}}$	135	mM	Neuronal potassium concentration of the effective flux
$[\mathbf{K^+}]_{\mathbf{O\_0}}$	3.5	mM	Extracellular potassium concentration of the effective flux
$[\mathbf{K^+}]_{\mathbf{A\_0}}$	135	mM	Astrocytic potassium concentration of theeffective flux
$[\mathbf{Na^+}]_{\mathbf{N\_0}}$	12.0	mM	Neuronal sodium concentration of the effective flux
$[\mathbf{Na^+}]_{\mathbf{O\_0}}$	144	mM	Extracellular sodium concentration of the effective flux
$[\mathbf{Na^+}]_{\mathbf{A\_0}}$	7.0	mM	Astrocytic sodium concentration of the effective flux

7

Model description

The mathematical description of I_K and I_{Na} were achieved through a Hodgkin-Huxley style derivation of forward and backward rate equations[1,2]:

$$I_K = g_K \cdot n^4 \cdot (V_n - E_{Kn})$$

$$I_{Na} = g_{Na} \cdot m^3 \cdot h \cdot (V_n - E_{Nan})$$

where g_K and g_{Na} are the conductance of fast Na^+ and K^+ channel; E_{Kn} and E_{Nan} are the neuronal equilibrium potential for K^+ and Na^+. The gate variables m, h, and n are dimensionless activation and inactivation variables, which describe the activation and inactivation processes of the sodium and potassium channels, each of which is governed by the following differential equations:

$$dn/dt = \alpha_n(V_n) \cdot (1 - n) - \beta_n(V_n) \cdot n$$

$$dm/dt = \alpha_m(V_n) \cdot (1 - m) - \beta_m(V_n) \cdot m$$

$$dh/dt = \alpha_h(V_n) \cdot (1 - h) - \beta_h(V_n) \cdot h$$

where the forward and the backward rate α and β describe the transition between the closed and open state of gate. The function of α and β are given by:

$$\alpha_n(V_n) = 0.01 \cdot (V_n + 55)/(1 - \exp[(-V_n - 55)/10])$$

$$\beta_n(V_n) = 0.125 \cdot \exp[(-V_n - 65)/80]$$

$$\alpha_m(V_n) = 0.1 \cdot (V_n + 40)/(1 - \exp[(-V_n - 40)/10])$$

$$\beta_m(V_n) = 4 \cdot \exp[(-V_n - 65)/18]$$

$$\alpha_h(V_n) = 0.07 \cdot \exp[(-V_n - 65)/20]$$

$$\beta_h(V_n) = 1/(\exp[(-V_n - 35)/10] + 1)$$

The neuronal membrane potential is highly dependent on the neuronal equilibrium potential for K^+ and Na^+, which are given by the Nernst equations:

$$E_{Kn} = R \cdot T/F \cdot \ln([K^+]_O/[K^+]_N)$$

$$E_{Nan} = R \cdot T/F \cdot \ln([Na^+]_O/[Na^+]_N)$$

where $[K^+]_N$ and $[K^+]_O$ are the neuronal and extracellular K^+ concentration; $[Na^+]_N$ and $[Na^+]_O$ are the neuronal and extracellular Na^+ concentration; R, T and F are the gas constant, absolute temperature and faraday constant.

Neuronal leak current is described by:

$$I_{Leak,N} = g_{Leak,N} \cdot (V_n - E_{Leak,N})$$

where $g_{Leak,N}$ is the neuronal leak conductance and $E_{Leak,N}$ is the neuronal leak potential.

The formula of Kir4.1 channel was modified from a previous model[3]:

$$I_{Kir} = g_{Kir} \cdot \sqrt{[K^+]_o} / (1 + \exp((V_A + V_{restA} - E_{Ka} + V_h)/V_S))(V_A + V_{restA} - E_{Ka})$$

$$I_{Kir\_vess} = g_{Kir\_vess} \cdot \sqrt{[K^+]_{O\_0}} / \left(1 + \exp\left((V_A + V_{restA} - E_{Ka\_vess} + V_h)/V_S\right)\right)(V_A + V_{restA} - E_{Ka\_vess})$$

where g_{Kir} and $g_{Kir_{vess}}$ are the conductance of Kir4.1 channel on the extracellular and vessel side respectively.

Astrocytic equilibrium potential for K^+ and Na^+ are given by:

$$E_{Ka} = R \cdot T/F \cdot \ln([K^+]_o/[K^+]_A)$$

$$E_{Naa} = R \cdot T/F \cdot \ln([Na^+]_o/[Na^+]_A)$$

where $[K^+]_A$ and $[Na^+]_A$ are the astrocytic K^+ and Na^+ concentration.

The astrocyte membrane potential equation also comprises a leak term:

$$I_{Leak,A} = g_{Leak,A} \cdot (V_A - E_{Leak,A})$$

The equation of the Na^+/K^+ pump depends on the extracellular K^+ and intracellular Na^+ concentrations as:

$$i_{pump,N} = i_{max,N} \cdot (1 + km_k/[K^+]_o)^{-2} \cdot (1 + km_{Na}/[Na^+]_N)^{-3}$$

$$i_{pump,A} = i_{max,A} \cdot (1 + km_k/[K^+]_o)^{-2} \cdot (1 + km_{Na}/[Na^+]_A)^{-3}$$

where $i_{max,N}$ and $i_{max,A}$ are the Na^+/K^+ pump rate for neuron and astrocyte respectively.

The kinetics of ion concentrations are calculated as:

$$d[K^+]_o/dt = (I_{Kir} + I_K)/(F \cdot Vol_o) - 2i_{pump,A} - 2i_{pump,N} - d_{K\_O} \cdot ([K^+]_o - [K^+]_{O\_0})$$

$$d[K^+]_N/dt = -I_K/(F \cdot Vol_N) + 2i_{pump,N} \cdot Vol_O/Vol_N - d_{K\_N} \cdot ([K^+]_N - [K^+]_{N\_0})$$

$$d[K^+]_A/dt = (-I_{Kir} - I_{Kir\_vess})/(F \cdot Vol_A) + 2i_{pump,A} \cdot Vol_O/Vol_A - d_{K\_A} \cdot ([K^+]_A - [K^+]_{A\_0})$$

$$d[Na^+]_o/dt = I_{Na}/(F \cdot Vol_o) + 3i_{pump,A} + 3i_{pump,N} - d_{Na\_O} \cdot ([Na^+]_o - [Na^+]_{O\_0})$$

$$d[Na^+]_N/dt = -I_{Na}/(F \cdot Vol_N) - 3i_{pump,N} \cdot Vol_O/Vol_N - d_{Na\_N} \cdot ([Na^+]_N - [Na^+]_{N\_0})$$

$$d[Na^+]_A/dt = -3i_{pump,A} \cdot Vol_O/Vol_A - d_{Na\_A} \cdot ([Na^+]_A - [Na^+]_{A\_0})$$

where Vol_O, Vol_N and Vol_A are the volumes of the extracellular, neuronal and astrocytic compartments. The term $d \cdot ([X] - [X_0])$ accounts for the diffusion effect, where d is the rate of this effective flux, [X] is the ionic concentration and $[X_0]$ is the equilibrium concentration.

Simulations were solved numerically with an explicit Runge-Kutta Prince-Dormand 8th-9th order method with the GSL library in cython and python. The parameters used in the model are presented in Supplementary Table 1.

References

1 Abbott, L. F. & Kepler, T. B. in *Statistical Mechanics of Neural Networks: Proceedings of the Xlth Sitges Conference Sitges, Barcelona, Spain, 3–7 June 1990* (ed Luis Garrido) 5-18 (Springer Berlin Heidelberg, 1990).

2 Gerstner, W. & Kistler, W. M. *Spiking neuron models : single neurons, populations, plasticity*. (Cambridge University Press, 2002).

3 Sibille, J., Dao Duc, K., Holcman, D. & Rouach, N. The neuroglial potassium cycle during neurotransmission: role of Kir4.1 channels. *PLoS computational biology* **11**, e1004137 (2015).